J. Appl. Comput. Mech., 12(1) (2026) 309-330
DOI: 10.22055/jacm.2025.48415.5217

ISSN: 2383-4536
jacm.scu.ac.ir

Shahid Chamran University of Ahvaz

Journal of Applied and Computational Mechanics

Research Paper

Effect of Slot Jet on Heat Transfer and Flow Characteristics of Microchannel Heat Sink Partially Filled with Porous Media at High Heat Flow Density and Conjugate Heat Transfer Boundary Conditions

Hongyu Pan[1], Yijie Zhuang[1], Wenhui Fan[2], Fengquan Zhong[2,3]

[1] School of Environmental Science and Engineering, Guangdong University of Technology, Guangzhou, 510006, China
[2] State Key Laboratory of High Temperature Gas Dynamics, Institute of Mechanics, Chinese Academy of Sciences, Beijing 100190, China
[3] School of Engineering Science, University of Chinese Academy of Sciences, Beijing 100049, China

Received April 30 2025; Revised June 16 2025; Accepted for publication June 19 2025.
✉ Corresponding authors: Y. Zhuang (zyj7933@gdut.edu.cn); W. Fan (fanwenhui@imech.ac.cn)

Abstract. In this paper, a three-dimensional mathematical model of microchannel heat sink slot jet partially filled with porous media coupled heat transfer is constructed with the local thermal non-equilibrium (LTNE) model and the Darcy-Forchheimer model, taking into account the buoyancy effect and the conjugate heat transfer boundary conditions. Copper foam metal is employed as the porous medium substrate and SIMPLE algorithm is used to solve the mathematical model. The coupled effects of porosity (ε), Reynolds number (Re) and thickness of the porous region (h) on the flow and temperature fields are comprehensively evaluated. The numerical results show that for all the cases, the temperature distribution of the fluid and porous medium is not consistent, and the temperature of porous medium is lower in the region perpendicular to the jet inlet due to the stagnation point effect. As the porosity increases from 0.35 to 0.50, the total average Nusselt number on the upper surface decreases from 46.85 to 13.12, while the total average Nusselt number at the interface increases from 2.13 to 2.98. High speed fluids are more prone to deflection after impacting porous media, and the faster the flow velocity inside the square cavity, the easier it is to form a high-speed channel in the middle. The formation of high-speed channel to drive the lower part of the square cavity flow rate, the vortex becomes more flatter and longer, convection heat transfer effect is enhanced. Meanwhile, as the thickness of the porous layer increases, the heat of the porous medium can be easily transferred to the fluid, resulting in an increase in the overall temperature of the square cavity and a larger temperature gradient on the upper surface. The results may provide design ideas for microchannel heat sinks for electronic components.

Keywords: High heat flow density, Conjugate heat transfer, Slot jet microchannel heat sink, Partially filled with porous media, Standing point effect.

1. Introduction

With the advancement of micro- and nanofabrication technology, high performance chips are becoming increasingly integrated and compact [1], playing a significant role in a range of fields, including communications, energy, the environment, and aerospace [2-4]. In accordance with the technology roadmap of electronics manufacturing [5], the mean heat flux of electronic components in 2020 has reached 500 W/cm², and this value will increase in the hotspot area. Local hotspots can lead to overheating and large temperature gradients (e.g., 5 K-30 K), which leads to a sharp reduction in the signal-to-noise ratio and a rapid deterioration in chip performance and reliability [6]. Furthermore, research has demonstrated that an increase of 10°K in the temperature of a chip results in a twofold increase in the failure rate of electronic devices, with 55% of the failures caused by excessively high operating temperatures [7]. As current demand for more powerful chips in smaller packages grows, electronic components must operate within a reasonable temperature range to ensure the reliability, safety and performance of electronic devices [8]. However, traditional chip thermal management solutions can no longer meet current demands, and issues such as microchip integration and high dissipation rates remain to be addressed. Consequently, there is a pressing need for the development of advanced thermal management techniques to improve heat dissipation efficiency and provide conditions for the normal operation of electronic components.

Since the microchannel heat sinks (MCHS) was first proposed by Tuckerman and Pease in 1981, it has received widespread attention due to its strong compactness, good temperature uniformity and adaptability [9]. Over the years, there has been a great deal of research into the improvement of the heat transfer performance of original microchannel models. For example, by modifying

Published online: June 23 2025

the microchannel structure and increasing the fluid disturbance within the microchannel to improve the convective heat transfer efficiency, the heat transfer performance of MCHS has been significantly improved [10-12]. Other common methods used to improve thermal and hydrodynamic performance of microchannel are summarized by Xie et al. [13], Sidik et al. [14] and Dixit and Ghosh [15]. These include (1) modification of microchannel structure and aspect ratio, (2) use of different shapes of microchannels and fins, (3) jet impingement, and (4) filling of the porous medium, as detailed in the following.

To improve the heat transfer efficiency and hydrodynamic performance of the heatsink, researchers investigated MCHS with different channel sizes and aspect ratios. Mudhafar and Xu [16] experimentally investigated the fluid flow and heat transfer characteristics on uncoated and microporous straight heat exchangers for high-power electronic devices, and showed that uncoated heat exchangers with 2 mm and 5 mm runner depths had the lowest thermal resistance at 30.6 W/cm^2 and 53.5 W/cm^2 heat fluxes, with 0.041°C/W and 0.027°C/W. Naphon et al. [17] experimentally investigated the effect of different MCHS aspect ratios on heat transfer and pressure drop under constant heat flux conditions and found that the average heatsink temperature was lower at higher channel heights due to the increased surface area and surface roughness. Furthermore, some researches about the traditional MCHS model proposed a manifold microchannel heat sink concept (MMC) [18], which was based on the original microchannel fluid "one-in-one". This resulted in a transition from an "in-out" flow mode to a "multiple-in-multiple-out" mode, which not only shortened the flow distance of the fluid in microchannel and reduced the overall pressure drop of the system, but also combines the advantages of shock jet. This further strengthened the heat transfer by intensifying the disturbance of the fluid [19].

An additional method of improving the heat transfer performance of microchannels is the modification of the configuration of the fins or the microchannels themselves [20]. Chai et al. [21] introduced staggered rectangular fins in microchannels to study the flow characteristics with different flow regimes and stronger perturbations in microchannels. A total of five distinct fin shapes were designed, including rectangular, isosceles triangular, rear triangular, front triangular and semi-circular. The objective was to impede the formation of a boundary layer within microchannels and enhance the efficiency of heat transfer. The simulation results demonstrated that the thermal performance of the microchannel heat sink with forward-facing triangular ribs was optimal at Reynolds numbers below 350. At Reynolds numbers exceeding 400, the semicircular ribs exhibited the most efficient heat transfer characteristics [22, 23]. Zhuang et al. [24] numerically investigated the heat sink flow and heat transfer characteristics of composite honeycomb microchannels for phase change materials, and the results showed that the design of honeycomb inflow structure and the thermal management characteristics of PCM phase change cooling resulted in better temperature uniformity and cooling performance. For two-phase flow heat transfer under certain conditions, Sempertegui-Tapia and Ribatski [25] and Zheng et al. [26] concluded that both triangular and circular microchannels had good heat transfer performance under high heat flux conditions, while circular microchannels were more suitable for low heat flux applications.

However, the above studies mainly focus on refining microchannel/fin dimensions and optimizing structures. While these approaches can enhance fluid perturbation and heat transfer, they cannot fundamentally solve the drawbacks of the traditional microchannels such as uneven flow distribution, large pressure gradient along the flow direction, and temperature inhomogeneity. To overcome these problems, researchers proposed microchannel cooling combined with jet impingement [27-30]. Compared with microchannel cooling, jet impingement disturbs the boundary layer more sufficiently due to the presence of the stagnation point effect and produces better local heat transfer performance, especially for hotspots [28, 31]. Peng et al. [28] designed a multi-jet microchannel (MJMC) heat sink where the coolant was ejected in the direction normal to the heated surface thereby replacing the inlet and outlet flow, and it was found that the MJMC with a higher number of nozzles, wider outlet, and a smaller fin width to channel width ratio had better cooling performance. Zhang et al. [32] investigated the effect of microchannel shape on microchannels and slot jets and found that with the same flow rate, circular microchannels combined with jet mode had the largest pressure drop, while trapezoidal channels had the best cooling performance, and the cooling advantage of trapezoidal channels increased as the incident flow rate increased. Shen et al. [33] investigated topology-optimized microchannel heat sinks integrated with impingement jets. Both simulation and experimental results showed that among the six test samples with Reynolds numbers ranging from 55.28 to 497.52, the model with the coolant inlet set on the same side of the microchannel and containing horizontal and inclined fins performed the best in terms of heat transfer efficiency.

Jet impingement improves heat transfer performance in local areas, but the pressure drop loss due to the impact is large and the overall improvement in heat transfer efficiency is not significant. To address this issue, some researchers proposed the use of metallic porous media to improve the effective thermal conductivity and increase the convective heat transfer area to improve the heat transfer performance within the microchannels [34, 35]. For the study of heat transfer properties of metallic porous media, Zhang and Huang et al. [36-38] investigated the melting heat transfer and energy storage properties of foam-metal composites using Darcy-Forchheimer and local thermal non-equilibrium models. In order to study the heat transfer performance of porous media, Bernardo et al. [34] analyzed the heat transfer characteristics of fully filled porous media in microchannels with slot jet by considering the buoyancy effect and using a local thermal non-equilibrium model. The findings indicated that porous media near the surface of heat source exhibited a markedly enhanced heat transfer effect, with higher thermal conductivity resulting in superior heat transfer performance within the porous media [34, 39]. Fully filled porous media significantly improves heat transfer but results in a greater pressure drop, which can be effectively improved by partially filled porous media. Hwang [40] and Dórea et al. [41] investigated the heat transfer characteristics of slot jets with partially filled porous media. Their findings revealed that partially filling the channel with porous media could modulate the flow field and heat transfer performance in the channel, while the average Nusselt number increased with the increase of Reynolds number. In addition, Cicek and Baytas [42] investigated the impact heating of nanofluid jets on a cooled surface with constant heat flux and observed that the local temperature variation increased along the upper wall with increasing Reynolds number, Darcy number and Grashof number. Kashkuli et al. [43] investigated numerically the impact of a liquid jet through a porous metal foam filled cooling channel. The results indicated the advantage of utilizing copper foam with 0.86 porosity and circular jet impingement.

In summary, the partially filled porous media microchannel jet cooling method not only strengthens the perturbation inside the microchannel and improves the heat transfer efficiency, but also combines the advantages of porous media heat transfer while reducing the pressure drop, which is a promising cooling method. However, most of the previous studies on microchannel porous media with slot jets used two-dimensional numerical simulation, and the studies on three-dimensional partially filled porous media with slot jets were not enough. Meanwhile, previous studies have not sufficiently discussed the conjugate heat transfer conditions and lacked a systematic description of the flow and heat transfer characteristics at the interface between the porous medium and the free-flow region. Therefore, in this paper, a three-dimensional mathematical model for flow and heat transfer of a microchannel heat sink slot jet partially filled with porous media is constructed. The finite volume method is employed to construct the model, and the SIMPLE algorithm is used to solve it. This heat sink could be applied to the thermal management of electronic components, taking into account the buoyancy effect and the conjugate heat transfer boundary conditions, and combining the local thermal non-equilibrium (LTNE) model and the Darcy-Forchheimer model to explain the heat transfer and flow characteristics within the microchannel partially filled porous media. On this formation, the coupled effects of porosity, Reynolds number and thickness of the porous region on the flow and temperature fields are comprehensively evaluated. The results of this study may provide a theoretical and practical basis for solving the flow and heat transfer problems of porous media in microchannel heat dissipation.

2. Mathematical Model

2.1. Problem description

Figure 1(a) shows a physical model of a microchannel heat sink slot jet partially filled with porous media. The cavity can be considered as a section of the jet in the microchannel. In this case, copper foam metal is used as the porous medium substrate, which is loaded with constant high heat flux in the upper surface, and non-porous medium region and slot jets are presented in the lower part of the porous medium. The specific dimensions of the square cavities were dimensionless. The length, width and height of the cavity are n × 2n × n (x × y × z), and the upper part of the cavity is filled with a porous copper foam medium with a thickness of h, where the PPI (pores per inch) of the copper foam is 10. The lower part of the cavity is a free-flowing non-porous media region. A slot jet inlet (length: n, width: 0.1n) is placed on the lower surface of the cavity, and cooling water are vertically ejected from the slot at a uniform velocity of w_{in} and a uniform temperature of T_∞, while the upper surface of the cavity is loaded with continuous high heat flux (500 W/cm²). To simplify the calculation, the left surface of the cavity is the symmetric boundary, the right surface is fully developed free-flow outlet and the other surfaces remain adiabatic. The relevant physical parameters of the copper foam and cooling water are given in Table1. The complete microchannel heat sink structure, specific dimensions, and application scenarios are shown in Fig. 1(b).

To establish the mathematical model, some assumptions are clarified as follows:

(1) Cooling water is considered as incompressible fluid. The change in density of cooling water follows the Boussinesq assumption when buoyancy effects are considered [39]. Since the temperature change is not drastic, it is assumed that the thermophysical properties of the fluid and the copper foam porous medium are constant.
(2) The flow in microchannels is single-phase, fully developed, and stably laminar. Copper foam porous media are regarded as continuous and isotropic [44], and the Darcy-Forchheimer model is employed in the momentum conservation equation to elucidate the flow and seepage characteristics in porous media.
(3) The LTNE model is employed to elucidate the phenomenon of heat transfer between a fluid and a porous medium, while neglecting the influence of radiative heat transfer and viscous heat dissipation.

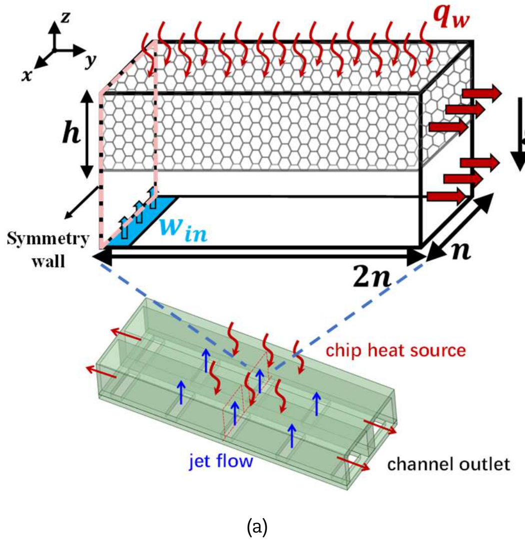

(a)

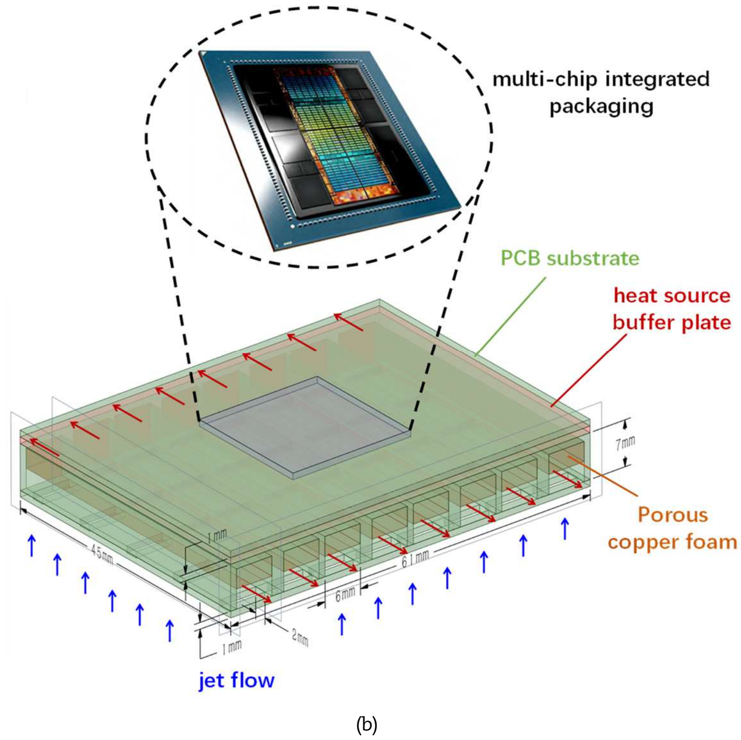

(b)

Fig. 1. (a) Schematic diagram of microchannel square cavity structure (dimensionless), (b) The complete microchannel heat sink structure and application scenarios.

Table 1. Thermophysical properties of cooling water and copper.

Properties	Water	Copper
Density (kg/m³)	1000	8920
Specific heat capacity (J/kg.K)	4186	380
Thermal conductivity (W/m.K)	0.58	401

2.2. Governing equations

Based on the above assumptions, a mathematical model of microchannel partially filled porous media slot jet coupled heat transfer is established. The governing equations are as follows [45, 46]:

Continuity equation:

$$\frac{\partial(\rho_f u)}{\partial x}+\frac{\partial(\rho_f v)}{\partial y}+\frac{\partial(\rho_f w)}{\partial z}=0. \tag{1}$$

Momentum equations:

$$\frac{\rho_f}{\varepsilon}\left[\frac{\partial u}{\partial t}+\frac{1}{\varepsilon}\frac{\partial(uu)}{\partial x}+\frac{1}{\varepsilon}\frac{\partial(vu)}{\partial y}+\frac{1}{\varepsilon}\frac{\partial(wu)}{\partial z}\right]=-\frac{\partial p}{\partial x}+\frac{\mu}{\varepsilon}\left(\frac{\partial^2 u}{\partial x^2}+\frac{\partial^2 u}{\partial y^2}+\frac{\partial^2 u}{\partial z^2}\right)-\lambda\left(\frac{\mu}{K}+\frac{\rho_f C}{\sqrt{K}}\sqrt{u^2+v^2+w^2}\right)u, \tag{2}$$

$$\frac{\rho_f}{\varepsilon}\left[\frac{\partial v}{\partial t}+\frac{1}{\varepsilon}\frac{\partial(uv)}{\partial x}+\frac{1}{\varepsilon}\frac{\partial(vv)}{\partial y}+\frac{1}{\varepsilon}\frac{\partial(wv)}{\partial z}\right]=-\frac{\partial p}{\partial y}+\frac{\mu}{\varepsilon}\left(\frac{\partial^2 v}{\partial x^2}+\frac{\partial^2 v}{\partial y^2}+\frac{\partial^2 v}{\partial z^2}\right)-\lambda\left(\frac{\mu}{K}+\frac{\rho_f C}{\sqrt{K}}\sqrt{u^2+v^2+w^2}\right)v, \tag{3}$$

$$\frac{\rho_f}{\varepsilon}\left[\frac{\partial w}{\partial t}+\frac{1}{\varepsilon}\frac{\partial(uw)}{\partial x}+\frac{1}{\varepsilon}\frac{\partial(vw)}{\partial y}+\frac{1}{\varepsilon}\frac{\partial(ww)}{\partial z}\right]=-\frac{\partial p}{\partial z}+\frac{\mu}{\varepsilon}\left(\frac{\partial^2 w}{\partial x^2}+\frac{\partial^2 w}{\partial y^2}+\frac{\partial^2 w}{\partial z^2}\right)-\lambda\left(\frac{\mu}{K}+\frac{\rho_f C}{\sqrt{K}}\sqrt{u^2+v^2+w^2}\right)w+(\rho\beta)_f g\left(T_f-T_\infty\right), \tag{4}$$

Energy equations, for cooling water:

$$\varepsilon(\rho c_p)_f\frac{\partial T_f}{\partial t}+(\rho c_p)_f\left(u\frac{\partial T_f}{\partial x}+v\frac{\partial T_f}{\partial y}+w\frac{\partial T_f}{\partial z}\right)=\varepsilon\left(k_{fe}+k_{td}\right)\left(\frac{\partial^2 T_f}{\partial x^2}+\frac{\partial^2 T_f}{\partial y^2}+\frac{\partial^2 T_f}{\partial z^2}\right)+\lambda h_{sf}a_{sf}\left(T_s-T_f\right), \tag{5}$$

For copper foam:

$$(1-\varepsilon)\left(\rho c_p\right)_s\frac{\partial T_s}{\partial t}=k_{se}\left(\frac{\partial^2 T_s}{\partial x^2}+\frac{\partial^2 T_s}{\partial y^2}+\frac{\partial^2 T_s}{\partial z^2}\right)-h_{sf}a_{sf}\left(T_s-T_f\right). \tag{6}$$

where u, v, and w represent the velocity components in x, y, and z directions, respectively, t is the time, p is the pressure, and g is the gravitational acceleration. T_f, T_s, and T_∞ represent the fluid temperature, the copper foam porous medium temperature, and the external ambient temperature, respectively. ρ_f, ρ_s, c_f, c_s and β_f indicate cooling water density, copper foam density, cooling water specific heat capacity and copper foam specific heat capacity and thermal cooling water expansion coefficient, respectively. λ and ε are the porous region control parameters and porosity, determined by the following equations [42]:

$$\lambda=\begin{cases}0, & \text{in the clear region}\\ 1, & \text{in the porous region}\end{cases},\quad \varepsilon=\begin{cases}1, & \text{in the clear region}\\ \varepsilon, & \text{in the porous region}\end{cases}. \tag{7}$$

The third term on the right side of Eqs. (2)-(4) is the Darcy-Forchheimer expression [47], which describes the non-Darcy and inertial effects in copper foam porous media. Where K and C are the permeability and inertia coefficients, respectively, given by [48]:

$$K=\frac{\varepsilon^2}{36\chi(\chi-1)}{d_k}^2, \tag{8}$$

$$C=0.00212(1-\varepsilon)^{-0.132}\left(\frac{d_f}{d_p}\right)^{-1.63}. \tag{9}$$

Here, χ, d_k, d_p, d_f and ω are the bending coefficient, characteristic length, pore diameter, fibre diameter and *PPI* of the copper foam, respectively, which value determined by the following equation:

$$\chi=2+2\cos\left[\frac{4\pi}{3}+\frac{1}{3\cos(2\varepsilon-1)}\right], \tag{10}$$

$$d_k=\frac{\chi d_p}{(3-\chi)}, \tag{11}$$

$$d_f=1.18d_p\sqrt{\frac{1-\varepsilon}{3\pi}}, \tag{12}$$

$$d_p=\frac{22.4\times10^{-3}(m)}{\omega(\mathrm{PPI})}. \tag{13}$$

The fourth term on the right-hand side of Eq. (4) represents the buoyancy source term, which follows the Boussinesq assumption:

$$\rho=\rho_\infty\left[1+\beta_f\left(T-T_\infty\right)\right]. \tag{14}$$

The local thermal non-equilibrium model of Eqs. (5)-(6) is used to explain the heat transfer effect between the porous medium and the cooling fluid, because copper foam is a high thermal conductivity metal, so the determination of the effective thermal conductivity k_{eff} is particularly important. In this paper, the cellular model of porous foam metal established by Boomsma and Poulikakos [49] is used to obtain k_{eff}. For porous media at the microscopic pore scale, intermixed percolation of fluids within them leads to enhanced heat transfer. Its enhancement effect can be determined using the heat diffusion model created by Georgiadis and Catton's [50] for k_{td} given by:

$$k_{eff}=\frac{1}{\sqrt{2}\left(R_A+R_B+R_C+R_D\right)}, \tag{15}$$

$$R_A=\frac{4\sigma}{\left[2e^2+\pi\sigma(1-e)\right]k_s+\left[4-2e^2-\pi\sigma(1-e)\right]k_f}, \tag{16}$$

$$R_B=\frac{(e-2\sigma)^2}{(e-2\sigma)e^2k_s+\left[2e-4\sigma-(e-2\sigma)e^2\right]k_f}, \tag{17}$$

$$R_C=\frac{\sqrt{2}-2e}{\sqrt{2}\pi\sigma^2k_s+\left(2-\sqrt{2}\pi\sigma^2\right)k_f}, \tag{18}$$

$$R_D=\frac{2e}{e^2k_s+\left(4-e^2\right)k_f}, \tag{19}$$

$$k_{fe}=k_{eff}\,|_{k_s=0}, \tag{20}$$

$$k_{se}=k_{eff}\,|_{k_f=0}, \tag{21}$$

$$k_{td}=\frac{0.36}{1-\varepsilon}\rho_f c_f d_f\sqrt{u^2+v^2+w^2}. \tag{22}$$

where k_f, k_{fe}, and k_{se} are the thermal conductivity of cooling water, the effective thermal conductivity of cooling water, and the effective thermal conductivity of copper foam, respectively. σ and e are dimensionless constants denoted as:

$$\sigma=\sqrt{\frac{\sqrt{2}\left(2-\frac{3\sqrt{2}}{4}e^3-2\varepsilon\right)}{\pi\left(3-2\sqrt{2}e-e\right)}},\quad e=0.339.$$

In the second term on the right-hand side of the local thermal non-equilibrium equation of Eqs. (5)-(6), h_{sf} and a_{sf} are interfacial convective heat transfer coefficient and the interfacial surface area, respectively [46, 51]. They represent the heat transfer effect and heat transfer area between the fluid-solid. In this paper, the smooth cylindrical model of copper foam porous medium established by Zhukauskas [52] is used to determine them, one has:

$$h_{sf}=\begin{cases}0.76Re^{0.4}Pr^{0.37}\dfrac{k_f}{d_f},1\le Re\le 40\\ 0.52Re^{0.5}Pr^{0.37}\dfrac{k_f}{d_f},40\le Re\le 10^3\\ 0.26Re^{0.6}Pr^{0.37}\dfrac{k_f}{d_f},10^3\le Re\le 2\times 10^5\end{cases}, \tag{23}$$

$$a_{sf}=\frac{3\pi d_f}{d_p^2}. \tag{24}$$

The dimensionless variables are described below [42]:

$$X=\frac{x}{d_k},\quad Y=\frac{y}{d_k},\quad Z=\frac{z}{d_k},\quad P=\frac{p}{\rho_f w_{in}{}^2},\quad U=\frac{u}{w_{in}},\quad V=\frac{v}{w_{in}},\quad W=\frac{w}{w_{in}},$$

$$Re=\frac{w_{in}\cdot d_k}{\nu_f},\quad \tau=t\frac{w_{in}}{d_k},\quad \theta_f=\frac{T_f-T_\infty}{\Delta T},\quad \theta_s=\frac{T_s-T_\infty}{\Delta T},\quad \xi=\frac{\alpha_f}{\alpha_s},\quad \gamma=\frac{k_{fe}+k_{td}}{k_{se}},$$

$$H=\frac{h_{sf}a_{sf}d_k{}^2}{k_{fe}},\quad \Delta T=-\frac{d_k\Delta q_w}{k_{fe}},\quad Da=\frac{K}{d_k{}^2},\quad Pr=\frac{\nu}{\alpha_f},\quad Gr=\frac{gd_k{}^3\beta_f\Delta T}{\nu_f{}^2}.$$

where w_{in} is the velocity in the z-direction at the jet inlet (indicating a vertical jet), and ΔT is the temperature increment, which is related to the density of the heat flux. $\alpha_f=(k_{fe}+k_{td})/\rho_f c_f$ and $\alpha_s=k_{se}/\rho_s c_s$ indicate the effective diffusivity of the cooling water and the copper foam, respectively. Based on the above dimensionless variables, Eqs. (1)-(6) have the following dimensionless form:

$$\frac{\partial U}{\partial X}+\frac{\partial V}{\partial Y}+\frac{\partial W}{\partial Z}=0, \tag{25}$$

$$\frac{1}{\varepsilon}\frac{\partial U}{\partial \tau}+\frac{1}{\varepsilon^2}\left(\frac{U\partial U}{\partial X}+\frac{V\partial U}{\partial Y}+\frac{W\partial U}{\partial Z}\right)=-\frac{\partial P}{\partial X}+\frac{1}{\varepsilon Re}\cdot\left(\frac{\partial^2 U}{\partial X^2}+\frac{\partial^2 U}{\partial Y^2}+\frac{\partial^2 U}{\partial Z^2}\right)-\lambda\left(\frac{1}{DaRe}+\frac{C}{\sqrt{Da}}\sqrt{U^2+V^2+W^2}\right)U, \tag{26}$$

$$\frac{1}{\varepsilon}\frac{\partial V}{\partial \tau}+\frac{1}{\varepsilon^2}\left(\frac{U\partial V}{\partial X}+\frac{V\partial V}{\partial Y}+\frac{W\partial V}{\partial Z}\right)=-\frac{\partial P}{\partial Y}+\frac{1}{\varepsilon Re}\cdot\left(\frac{\partial^2 V}{\partial X^2}+\frac{\partial^2 V}{\partial Y^2}+\frac{\partial^2 V}{\partial Z^2}\right)-\lambda\left(\frac{1}{DaRe}+\frac{C}{\sqrt{Da}}\sqrt{U^2+V^2+W^2}\right)W+\frac{Gr}{Re^2}\theta_f. \tag{28}$$

$$\varepsilon\frac{\partial \theta_f}{\partial \tau}+\left(U\frac{\partial \theta_f}{\partial X}+V\frac{\partial \theta_f}{\partial Y}+W\frac{\partial \theta_f}{\partial Z}\right)=\varepsilon\frac{1}{Pr\cdot Re}\left(\frac{\partial^2 \theta_f}{\partial X^2}+\frac{\partial^2 \theta_f}{\partial Y^2}+\frac{\partial^2 \theta_f}{\partial Z^2}\right)+\lambda\frac{H}{Pr\cdot Re}\left[\theta_s-\theta_f\right], \tag{29}$$

$$(1-\varepsilon)\xi\frac{\partial \theta_s}{\partial \tau}=(1-\varepsilon)\frac{1}{Pr\cdot Re}\left(\frac{\partial^2 \theta_s}{\partial X^2}+\frac{\partial^2 \theta_s}{\partial Y^2}+\frac{\partial^2 \theta_s}{\partial Z^2}\right)+\gamma\frac{H}{Pr\cdot Re}\left[\theta_f-\theta_s\right]. \tag{30}$$

where *Re, Da, Pr, Gr* are Reynolds number, Darcy number, Prandtl number and Grashof number, respectively. ξ is the ratio of the effective diffusivity rate of the cooling water and copper foam. q_w is the heat flux density. H indicates the strength of the convective heat transfer capacity, which is related to the interfacial convective heat transfer coefficient, the interfacial surface area and the effective thermal conductivity of the water.

2.3. Conjugate heat transfer boundary conditions

In this study, the upper surface of the cavity is subjected to a continuous high heat flux density. It can be observed from Eq. (31) that the heat flow into the fluid and the copper foam is related to the porosity, which is expressed as follows [53]:

$$q_w=-\varepsilon k_{fe}\frac{\partial T_f}{\partial z}-(1-\varepsilon)k_{se}\frac{\partial T_s}{\partial z},\ T_s=T_f=T_{wall}. \tag{31}$$

Additionally, the approach of partially filling porous media is adopted to address the issue of heat transfer enhancement between microchannels, which inevitably contains the interface between porous and non-porous regions. As the dual-energy equations are solved separately, ensuring a suitable match between the temperature and heat flux at this interface is of paramount importance.

At the interface between the porous and non-porous regions, the equations for the heat flux q_{fluid} in the pure fluid region, the heat flux $q_{porous,f}$ in the fluid within the porous region and the heat flux $q_{porous,s}$ in the copper foam within the porous region are given by Costa et al. [54] and Mattos et al. [55]:

$$q_{fluid}\Big|_+=\left(-k_f\frac{\partial T_f}{\partial z}\right)\Bigg|_+, \tag{32}$$

$$q_{porous,f}\Big|_-=\left(-k_{fe}\varepsilon\frac{\partial T_f}{\partial z}\right)\Bigg|_-, \tag{33}$$

$$q_{porous,s}\Big|_-=\left[-k_{se}(1-\varepsilon)\frac{\partial T_f}{\partial z}\right]\Bigg|_-. \tag{34}$$

where the subscript + and subscript - represent the relevant parameters of the fluid/porous region, respectively.

The dual energy equations are solved individually, requiring that the flow and temperature fields of the fluid meet specific smoothness conditions, despite the fact that the material properties at the interface are not continuous [56]. Accordingly, the following compatibility conditions are implemented to guarantee that the calculated values are physically meaningful [57]:

$$T_{fluid}\Big|_+=T_{porous}\Big|_-, \tag{35}$$

$$\varepsilon q_{fluid}\Big|_+=q_{porous,f}\Big|_-, \tag{36}$$

$$(1-\varepsilon)q_{fluid}\Big|_+=q_{porous,s}\Big|_-. \tag{37}$$

The temperature and heat flux expressions can be collated from Eqs. (32)-(37) [58]:

$$T_{fluid}\Big|_+=T_{porous}\Big|_-=\left[\varepsilon T_f+(1-\varepsilon)T_s\right]_{porous}\Big|_-, \tag{38}$$

$$\left(-k_f\frac{\partial T_f}{\partial z}\right)\Bigg|_+=\left[-k_{fe}\varepsilon\frac{\partial T_f}{\partial z}-k_{se}(1-\varepsilon)\frac{\partial T_f}{\partial z}\right]\Bigg|_-. \tag{39}$$

In accordance with the aforementioned equations and dimensionless factors, the dimensionless boundary conditions presented in this study are as follows:

Initial and boundary conditions:

$$\tau = 0,\ \ U = V = W = 0,\ \ \theta_f = \theta_s = 0. \tag{40}$$

When $\tau \geq 0$, at upper surface (heat source):

$$\theta_f = \theta_s = \theta_{wall},\ \ U = 0,\ \ V = 0,,\ \ W = 0, \tag{41}$$

$$\varepsilon\frac{\partial\theta_f}{\partial Z} + (1-\varepsilon)\frac{1}{\gamma}\frac{\partial\theta_s}{\partial Z} = 1. \tag{42}$$

At the jet inlet:

$$\theta_f = \theta_{in} = 0,\ \ U = V = 0,\ \ W = W_{in} = 1. \tag{43}$$

At bottom surface (except jet inlet):

$$\frac{\partial\theta_f}{\partial Z} = 0,\ \ U = V = W = 0. \tag{44}$$

At symmetry surface:

$$\frac{\partial\theta_f}{\partial Y} = \frac{\partial\theta_s}{\partial Y} = \frac{\partial U}{\partial Y} = \frac{\partial Z}{\partial Y} = V = 0. \tag{45}$$

At outlet:

$$\frac{\partial\theta_f}{\partial Y} = \frac{\partial\theta_s}{\partial Y} = \frac{\partial U}{\partial Y} = \frac{\partial V}{\partial Y} = \frac{\partial W}{\partial Y} = 0. \tag{46}$$

At the front and rear surfaces:

$$\frac{\partial\theta_f}{\partial X} = \frac{\partial\theta_s}{\partial X} = 0,\ \ U = V = W = 0. \tag{47}$$

At the interface between porous and non-porous regions:

$$U_{fluid}\big|_+ = U_{porous,f}\big|_-,\ \ V_{fluid}\big|_+ = V_{porous,f}\big|_-,\ \ W_{fluid}\big|_+ = W_{porous,f}\big|_-, \tag{48}$$

$$\theta_{fluid}\big|_+ = \theta_{porous}\big|_- = \left[\varepsilon\theta_f + (1-\varepsilon)\theta_s\right]_{porous}\Big|_-, \tag{49}$$

$$\left(-k_f\frac{\partial\theta_f}{\partial Z}\right)\Bigg|_+ = \left[-k_{fe}\varepsilon\frac{\partial\theta_f}{\partial Z} - k_{se}(1-\varepsilon)\frac{\partial\theta_f}{\partial Z}\right]\Bigg|_-. \tag{50}$$

2.4. Data reduction

The velocity magnitude is defined as follows:

$$U_{total} = \sqrt{U^2 + V^2 + W^2}, \tag{51}$$

where U_{total} represents the velocity magnitude and U, V and W represent the dimensionless velocities in the X, Y, and Z axis directions, respectively.

The calculation of the Nusselt number is related to h_f, the convective heat transfer coefficient $h_{f|_{up}}$ at upper surface of square cavity is defined by the following equation:

$$h_{f|_{up}} = \frac{-q_w}{T_{wall} - T_\infty},\ \ T_s = T_f = T_{wall}. \tag{52}$$

Consequently, the expressions for the local Nusselt number at the upper surface of square cavity are obtained as:

$$Nu_{up} = \frac{h_{f|_{up}} d_k}{k_{fe}} = \frac{1}{\theta_{wall}}. \tag{53}$$

Similarly, the convective heat transfer coefficient $h_{f|_{middle}}$ and the local Nusselt number Nu_{middle} at the interface of the square cavity are obtained:

$$h_{f|_{middle}} = \frac{k_{fe}(\partial T_f / \partial y)}{T_f - T_\infty}, \tag{54}$$

$$Nu_{middle} = \frac{h_{f|_{middle}} d_k}{k_f} = \frac{k_{fe}}{k_f}\frac{\partial\theta_f}{\partial Z}. \tag{55}$$

The average Nusselt number is defined as follows:

$$\overline{Nu_{up}} = \frac{1}{A}\iint Nu_{up} dX dY, \tag{56}$$

$$\overline{Nu_{middle}} = \frac{1}{A}\iint Nu_{middle} dX dY. \tag{57}$$

3. Numerical Method and Verification

In this study, the finite volume method is used to solve the governing equations and the SIMPLE (Semi-Implicit Method for Pressure Linked Equations) algorithm is used to solve the staggered grid for the 3D flow field. In the staggered grid, the velocity components are stored at the centre of the grid and the scalars such as pressure and temperature are stored at the midpoint of the perpendicular plane normal to the centre of the grid. The numerical solution is terminated if the steady-state condition satisfies the following criterion:

$$\frac{\sum\left|\Phi^{m}_{i,j,k} - \Phi^{m-1}_{i,j,k}\right|}{\sum\left|\Phi^{m}_{i,j,k}\right|} \le 10^{-6}. \tag{58}$$

where m indicates the current iteration step, (i, j, k) the grid point, Φ the dependent variable (U, V, W, θ_f and θ_s). More details about the numerical algorithm can be found in Zhuang et al. [59].

In order to ensure the accuracy of the results, the grid-independent and time-independent solutions are verified. As shown in Fig. 2, the validation analyses were carried out for the number of grids (71824, 77452, 84525) and time steps (1.1×10^{-4}, 1.0×10^{-4}, 9.0×10^{-5}). It can be seen that the variation of Nusselt number with Y-axis distance is very close at different grid quantities (Fig. 2(a)) and different time steps (Fig. 2(b)). Therefore, to ensure computational accuracy and cost, the simulations in this study were carried out using a grid number of 77452 and a time step of 1.0×10^{-4}.

In order to ensure the accuracy of the simulation, the results of flow field with varied porous layer thickness were compared with the numerical results of Dórea [41] under the same working conditions ($Re = 750$, $Da = 8.28\times10^{-3}$, and $\varepsilon = 0.9$), as shown in Fig. 2(c) and Fig. 2(d), the flow field (streamline diagram) and temperature change curve obtained from the current simulation is basically consistent with the literature. Among them, the maximum relative error of the temperature in the y-direction is only 1.5%.

4. Results and Discussion

In current study, Prandtl number is fixed at $Pr = 7$, and Grashof number is fixed at $Gr = 10^4$. On this basis, the coupled effects of porosity (ε), Reynolds number (Re) and porous region thickness (h) on the flow and temperature fields were comprehensively evaluated.

4.1. Effects of porosity

The first section explores the effect of the change in porosity on the flow and heat transfer inside the square cavity. The three-dimensional distributions of flow and temperature field with $Re = 200$ and $h = n/2$ is shown in Fig. 3 and the flow and temperature field distributions in two different cross sections are shown in Figs. 4 and 5.

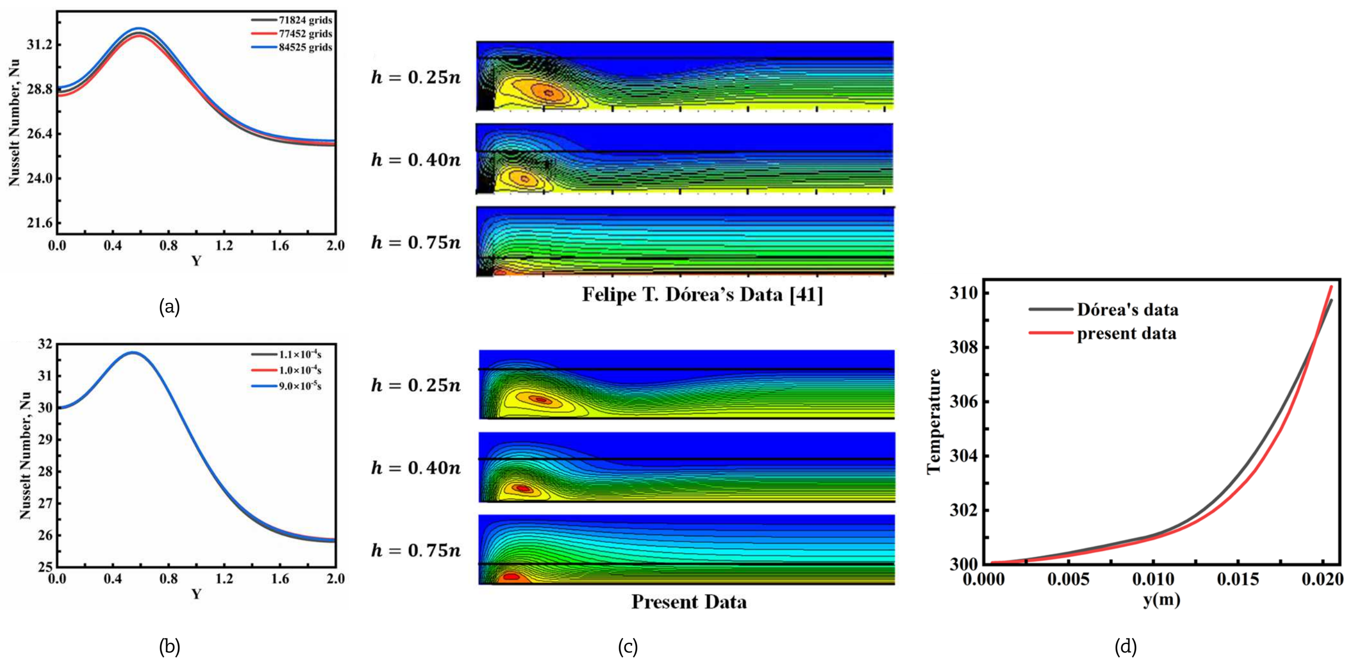

Fig. 2. (a) Grid-independent solutions, (b) Time-independent solutions, (c) Comparison of flow field between Dórea's [41] and the current results, (d) Comparison of temperature change curve between Dórea's [41] and the current results.

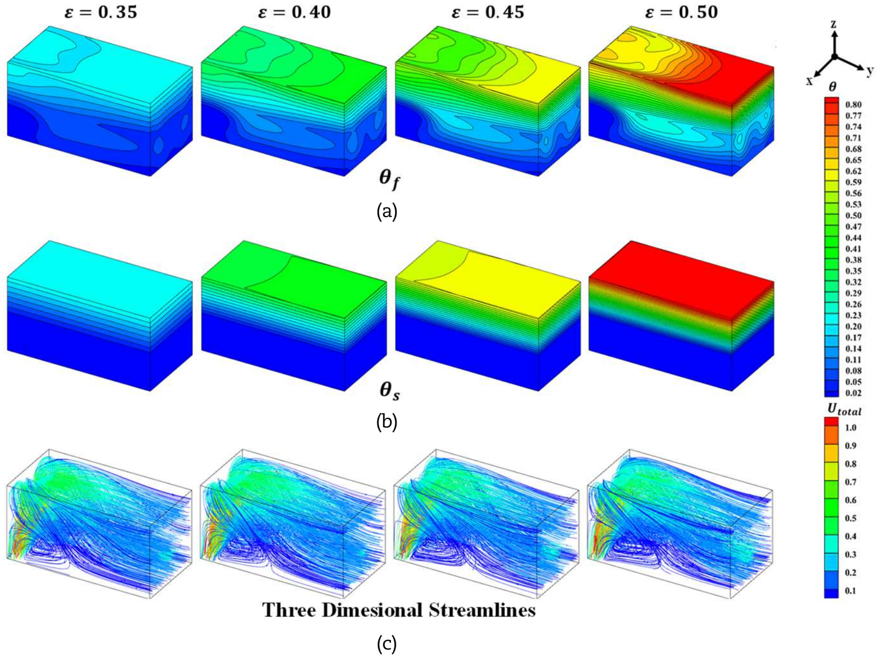

Fig. 3. Effect of porosity on (a) three-dimensional temperature distributions of the fluid, (b) three-dimensional temperature distributions of porous medium and (c) three-dimensional streamlines for *Re* = 200 and h = n/2.

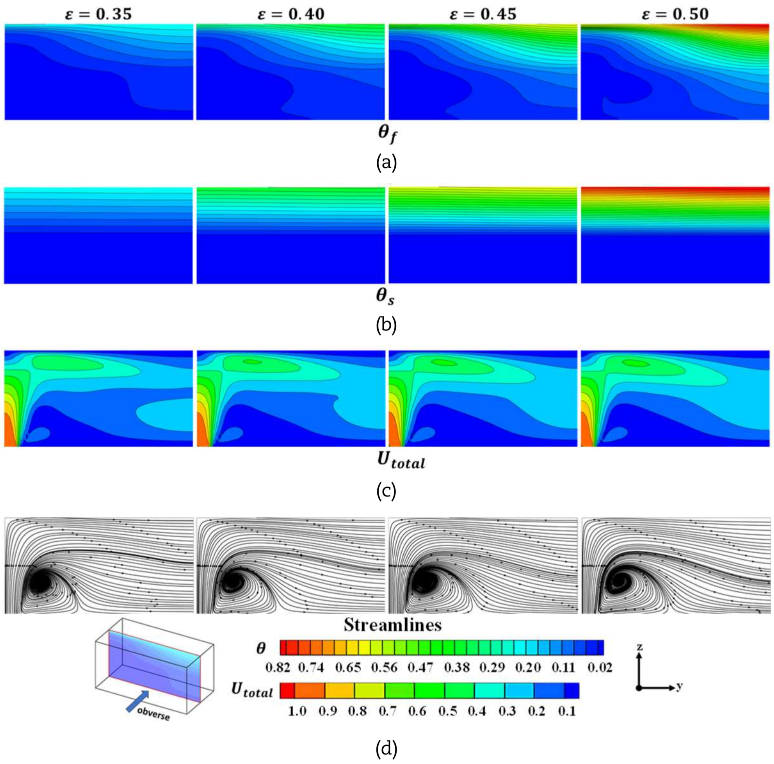

Fig. 4. Effect of porosity on (a) temperature distributions of the fluid, (b) temperature distributions of porous medium, (c) velocity distributions of the fluid and (d) streamlines for *Re* = 200 and h = n/2 at z-y observation section.

Figures 3(a) and 3(b) show the three-dimensional temperature distributions of the fluid and the porous medium, respectively. It can be observed in the temperature distribution plots of Figs. 3(a) and 3(b) that the temperature of the square cavity increases with increasing porosity and the temperature gradient becomes larger. The phenomenon can be attributed to the increase in porosity results in more through holes in the porous medium and a decrease in copper foam skeleton, which leads to a reduction in the effective thermal conductivity of the porous medium. At the same time in the upper surface of the square cavity loaded with a constant heat flux density, the reduction of the copper foam makes the action of the heat flux density of the fluid increases, and the fluid thermal conductivity is lower, so that the top of the heat cannot be transferred in a timely manner. In Fig. 3(a), it can be clearly seen that the fluid temperature is lower in the region perpendicular to the jet inlet, while the fluid temperature gradually increases along the y-axis (outlet) in the influence of the continuous heat flow on the upper surface. That is due to the stagnation point effect, the disruption of the temperature boundary layer is more pronounced in the region of jet impingement, which is able to produce a better localised heat transfer performance. Porosity does not strongly affect the flow behaviour of the fluid, as shown in the flow diagram of Fig. 3(c) and noted by Graminho and de Lemos [60].

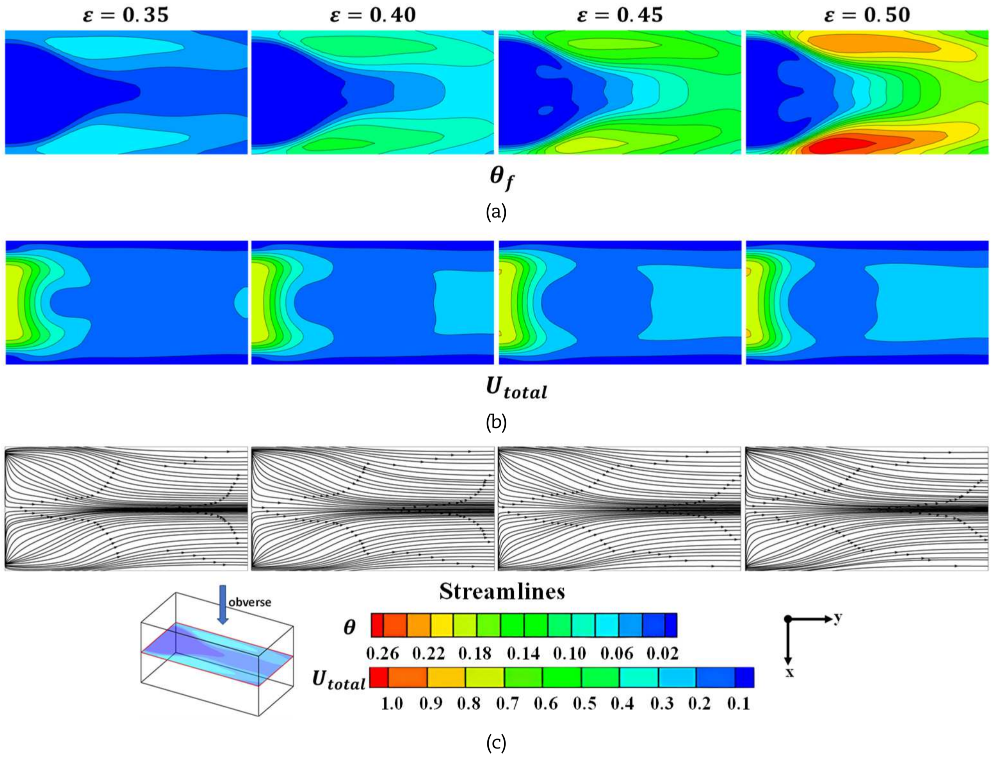

Fig. 5. Effect of porosity on (a) temperature distributions of the fluid, (b) velocity distributions of the fluid, and (c) streamlines for *Re* = 200 and h = n/2 at x-y observation section (interface).

In order to further investigate the flow and heat transfer characteristics on the porous media slot jet of microchannel, z-y and x-y observation sections inside the square cavity are selected. Figure 4 shows the temperature and flow fields at the z-y observation section inside the square cavity, and the same conclusions as in Fig. 3 can be observed in Figs. 4(a) and 4(b). The temperature difference between the fluid and solid regions of the porous medium is large and as the porosity increases, the temperature of the square cavity increases and the temperature gradient becomes larger. Differently, comparing Figs. 3(a) and 4(a), it can be seen that inside the square cavity, the temperature field of the observation section shows more low-temperature regions, especially in the region above the jet inlet. This is because that, in the inner region, the fluid is less affected by the stationary walls and the speed of vertical jet gets faster, so that more cooling medium can enter the upper part of the porous medium, the stagnation point effect is enhanced and the fluid-solid heat transfer is more efficient. Figures 4(c) and 4(d) show the flow field and streamlines at z-y observation section. As shown in Fig. 4(c), the increase in porosity makes the porous medium have more through holes, the fluid percolates sufficiently through the porous medium, the flow velocity increases, and the flow field presents fewer low velocity regions. In Fig. 4(d), it can be seen that the effect of porosity on the strength of the main vortex is less obvious, and the magnitude of the vortex increases slightly with the increase of porosity, meanwhile, the larger the porosity is, the more obvious the tendency of the streamline descends. The reason for these phenomena is that smaller porosity makes the fluid flow restricted, the vortex is not fully developed, and the streamlines show an upward trend under the combined effect of buoyancy and jet.

The conjugate heat transfer interface between the porous medium and the free-flow region is also the focus of this study, and Fig. 5 demonstrates the temperature and flow fields of the fluid at the interface. As seen in Fig. 5(a), overall fluid temperature increases along the y-axis under the influence of the slot jet and the density of the heat flow. Simultaneously, at the interface, the cooling medium is obstructed by the porous medium to form a vortex, and the vortex perturbation strengthens the heat exchange, which results in the formation of a conical low-temperature region from the jet. It is worth mentioning that in this simulation, the walls in the x-direction are set to be adiabatic and stationary, so the flow field at the interface shows a conical low-temperature region and low fluid temperature in the middle and high temperature at the wall. Figures 5(b) and 5(c) show the temperature field and streamlines at the interfaces, and in Fig. 5(b), it can be seen that the increase in porosity results in a sufficient fluid flow, and therefore the flow rate of the fluid at the exit of the higher porosity case is higher compared to the lower porosity case. As shown in the streamlines in Fig. 5(c), the change in porosity does not drastically influence the fluid flow, but only the streamlines become denser at the outlet due to the velocity field.

Next, Nusselt number and velocity magnitude are introduced to quantitatively analyze the heat transfer and flow characteristics inside the square cavity. In order to investigate the variation of the local Nusselt number and the local velocity magnitude inside the three-dimensional square cavity, area1 and area2 shown in schematic diagram of Fig. 6 were selected.

Figure 6(a) provides a combined analysis of the average Nusselt number for both surfaces. As the porosity increases from 0.35 to 0.50, the average Nusselt number on the upper surface decreases from 46.85 to 13.12, while the average Nusselt number at the interface increases from 2.13 to 2.98, and the average Nusselt number on the two surfaces shows an opposite trend. The upper surface directly contacts heat loading and the fluid velocity is lower on the top region, which causes that the heat transfer effect is mainly influenced by heat conduction. At higher porosity, the copper foam decreases, the heat flow directly acting on the fluid with lower thermal conductivity increases, and the effective thermal conductivity of the upper surface gets smaller, which results that the average Nusselt number decreases. However, at the interface, where the velocity of cooling medium is higher and the main vortex is fully developed, thus convective heat transfer dominates. At higher porosity, the reduction of copper foam allows more space for the fluid flowing, the main vortex becomes larger and convective heat transfer is enhanced, resulting in the average Nusselt number is elevated.

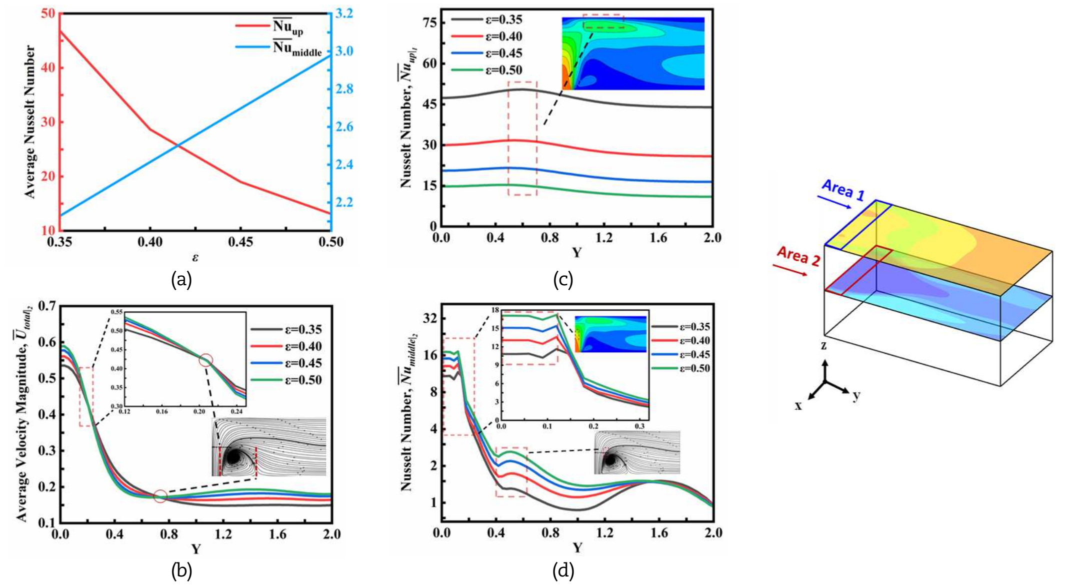

Fig. 6. Effect of porosity on (a) variation in average Nusselt number, (b) variation of velocity magnitude with Y-axis at interface, (c) variation of local Nusselt number with Y-axis at upper surface and (d) variation of local Nusselt number with Y-axis at interface for *Re* = 200 and h = n/2.

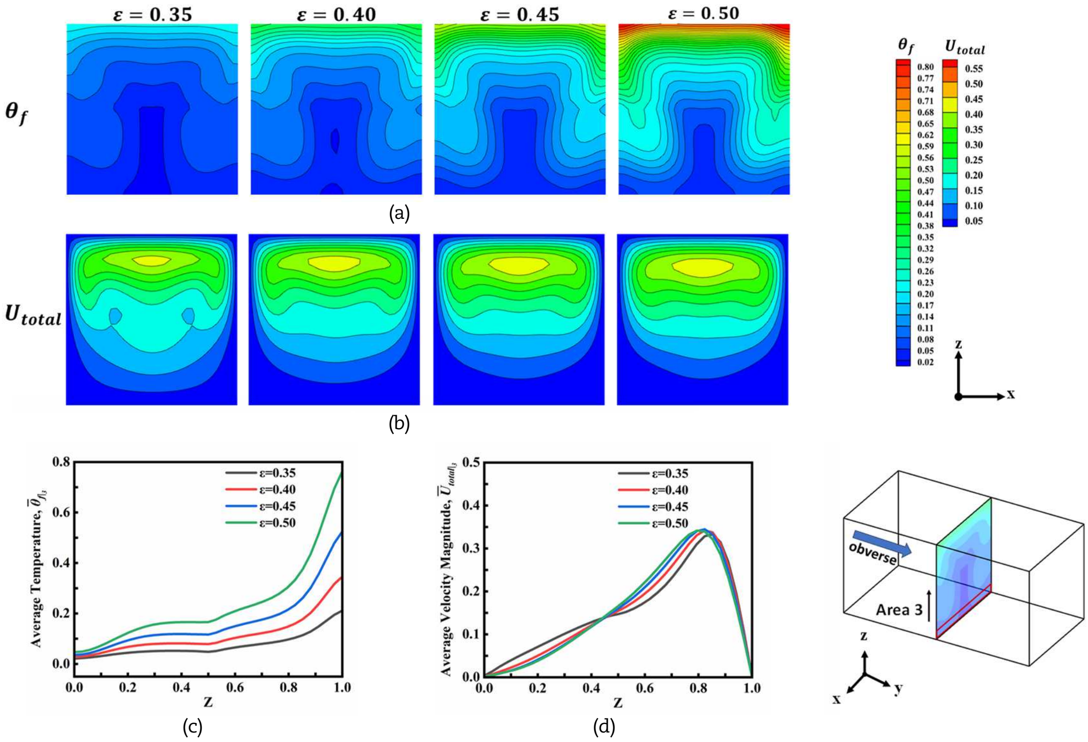

Fig. 7. Effect of porosity on (a) temperature distributions of the fluid, (b) velocity distributions of the fluid, (c) variation of fluid temperature with Z-axis and (d) variation of velocity magnitude with Z-axis for *Re* = 200 and h = n/2 at z-x observation section.

Figure 6(b) demonstrates the variation trend of the interfacial velocity magnitude along the Y-axis for different porosities. For all cases, there is an overall decreasing trend in the velocity magnitude along the Y-axis, and for the $\varepsilon = 0.50$ and $\varepsilon = 0.45$ cases, there is an increase in the velocity close to the outlet, which corresponds to the trend of the velocity contours shown in Fig. 5(b). It is worth noting that the two intersection points (Y = 0.21 and Y = 0.75) in the curve of Fig. 6(b) correspond exactly to the length of the main vortex, which indicates that the disturbance of the vortex has a significant effect on the flow velocity of the fluid at the interface. As the porosity increases, the vortex size increases slightly and the disturbance of the main vortex enhances the flow velocity in the tail of the vortex, resulting in increase in velocity near the outlet. As shown in Fig. 6(c), as previously analysed, the upper surface Nusselt number decreases with increasing porosity. However, due to the stagnation point effect, the jet fluid gradually decelerates after contacting the porous medium and percolates through the porous medium, eventually coming to a standstill at the upper wall surface. Stagnation point effect strengthens the disturbance to the thermal boundary layer, and thus the local Nusselt number of the upper surface reaches a peak in the region of Y = 0.6 (which corresponds to the region of higher flow velocity above the porous medium). Figure 6(d) shows the variation curve of the local Nusselt number at the interface with the Y-axis, in which the local Nusselt number at the interface reaches the peak in the region of Y = 0.13. In this region, the jet directly impacts the porous medium and the flow rate is fast, which enhances the convective heat transfer; and then as the flow rate decreases, the local Nusselt number also decreases to the vortex generation region (Y = 0.42) and fluctuates. It can be seen from the streamline diagram that the streamlines in the region of Y = 0.42 are denser, and the vortex perturbation enhances the convective heat transfer, which improves the local Nusselt number.

In order to analyse the flow and heat transfer characteristics inside the square cavity perpendicular to the Y-axis, a z-x observation section inside the square cavity is selected for analytical study. Figures 7(a) and 7(b) show the fluid temperature and velocity fields inside the square cavity perpendicular to the Y-axis (Y = 1) observation section. Figures 7(c) and 7(d) show the variation curves of the temperature and velocity magnitude of area 3 shown in schematic diagram of Fig. 7 along the Z-axis. Combining Fig. 7(a) with Fig. 7(c), similar conclusions to Fig. 3(a) can be observed: the fluid temperature and temperature gradient in the upper part of the square cavity increase with increasing porosity. Differently, Fig. 7(a) clearly demonstrates the presence of low-temperature channels in the region of free fluid flow, and the size of the low-temperature channels decreases with the increase of porosity. As shown in Fig. 7(b) and Fig. 7(d), the jet fluid is deflected by the combined action of the porous medium and the upper wall surface, and the velocity peaks at the upper part of the square cavity (Z = 0.8). It is worth pointing out that in Fig. 7(b), it is observed that there are more high-speed regions in the upper part of the square cavity with higher porosity (yellow part in the contours), while the regions with fast flow velocity in the lower part of the square cavity are reduced. That is because as the porosity decreases, the porous medium enhances the obstruction effect on the fluid. This leads to the phenomenon of high flow rate in the lower part of the square cavity with low porosity and high flow rate in the upper part of the square cavity with high porosity. It is more obvious in the flow field and the graphs for $\varepsilon = 0.35$.

4.2. Effects of Reynolds number

The second section explores the effect of Reynolds number on the flow and heat transfer inside the square cavity with same ε and h ($\varepsilon = 0.40$ and $h = n/2$). The flow and temperature field distributions in three dimensions is shown in Fig. 8 and the flow and temperature field distributions in two observation sections are shown in Fig. 9 and Fig. 10.

Figures 8(a) and 8(b) demonstrate the three-dimensional temperature distributions of the fluid and the porous medium, respectively. Comparing Fig. 8(a) and Fig. 8(b), it can be seen that because of the percolating characteristics of the fluid, the fluid temperature distribution is uneven, while the temperature field of the porous medium is more uniformly distributed, and its isotherms are regularly varying. Meanwhile, it can be observed in the temperature distribution contours of the fluid and porous medium that with the increase of the Reynolds number, the thermal boundary layer at the top of the square cavity becomes thicker and the temperature gradient becomes larger. As seen in Fig. 8(c), the higher the Reynolds number, the denser the streamlines in the middle of the square cavity, which indicates that the flow velocity is fast and the fluid flow is intense in this area. For the lower Reynolds number, the region with dense streamlines is shifted upward. Especially for the case of $Re = 200$, in the area of vertical jet inlet, the flow velocity is faster and the main vortex formed on the front and rear wall is smaller. For other cases, with the increase of Reynolds number, the wall vortex becomes flattened and elongated, resulting in denser streamlines in the middle. These three-dimensional streamlines also explain the temperature field phenomenon, the increase of the Reynolds number indicates that the inlet flow rate increases, and the high-speed fluid impacting porous medium is more likely to be deflected. So, the higher Reynolds number, the more-dense streamlines at the interface, the faster flow rate. This also makes the fluid into the upper part of the square cavity becomes less, the flow rate is reduced, weakened convective heat transfer, the upper surface temperature becomes higher, and the temperature gradient becomes larger.

To explore the effect of Reynolds number variation on the flow and temperature fields inside the square cavity, consistent with the previous text, z-y and x-y observation sections inside it were selected for the analytical study. Figure 9 shows the temperature field, flow field and streamlines at the z-y observation section inside the square cavity. In Fig. 9(a) and Fig. 9(b), the same conclusion as Fig. 8(a) can also be obtained: the temperature distribution of the fluid and the porous medium is inconsistent, and with the increase of the Reynolds number, the temperature of the upper part of the square cavity increases, the thermal boundary layer on the upper surface becomes thicker, and the temperature gradient becomes larger. Differently, comparing Fig. 9(a) and Fig. 8(a), it can be seen that the fluid inside the square cavity is less affected by the front and rear wall surfaces, and it can reach the interface between the fluid and the porous medium at a faster speed. This enhances the convective heat transfer, and thus the temperature field at the observation section manifests more low-temperature regions.

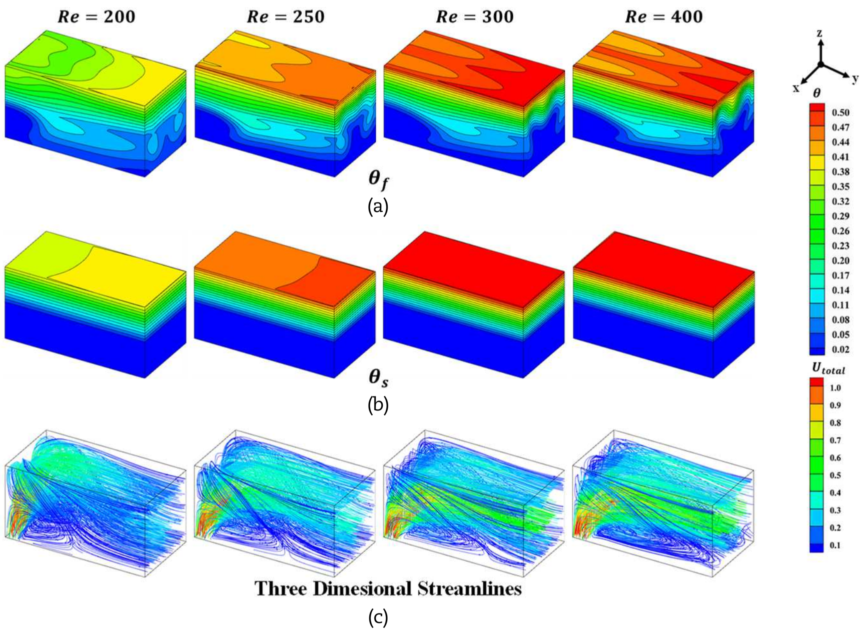

Fig. 8. Effect of Reynolds number on (a) three-dimensional temperature distributions of the fluid, (b) three-dimensional temperature distributions of porous medium and (c) three-dimensional streamlines for ε = 0.4 and h = n/2.

Figures 9(c) and 9(d) show the flow field and streamlines of the z-y observation section. As shown in Fig. 9(c), because the increase of the Reynolds number indicates the increase of the jet flow velocity, the high velocity fluid impacting the porous medium produces a deflection. So, the larger Reynolds number of the case, the faster the flow velocity inside the square cavity, the easier it is to form a high velocity channel in the middle, and the formation of the high velocity channel strengthens the convective heat transfer. The interfacial area is directly flushed by the high velocity channel, resulting in more intense fluid-solid heat transfer. However, the formation of the high velocity channel causes less fluid to enter the upper region, the flow rate decreases, the convective heat transfer is weakened, and the temperature increases at upper surface. The temperature field distribution can also be analyzed by above reason in Fig. 9(a) that, lower temperatures at the interface and higher temperatures at the top for the other Reynolds number cases compared to the case with $Re = 200$. It is worth pointing out that the formation of the high velocity channel drives the flow velocity in the lower part of the square cavity. For the larger Reynolds number, the flow velocity in the lower part of the square cavity is larger and the velocity field distribution shows a vortex-like shape, which is verified by the streamlines shown in Fig. 9(d). Figure 9(d) illustrates that the variation of Reynolds number has a significant effect on the intensity of the main vortex, and the increase of Reynolds number makes the vortex flattened and elongated, at the same time, the larger the Reynolds number of the case, the more likely that the deflection of the streamlines will occur earlier.

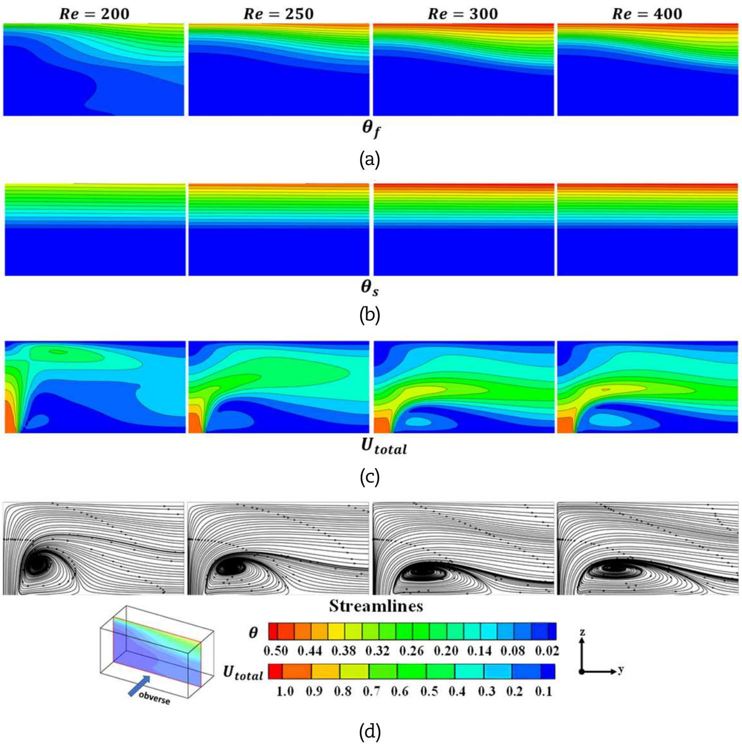

Fig. 9. Effect of Reynolds number on (a) temperature distributions of the fluid, (b) temperature distributions of porous medium, (c) velocity distributions of the fluid and (d) streamlines for ε = 0.4 and h = n/2 at z-y observation section.

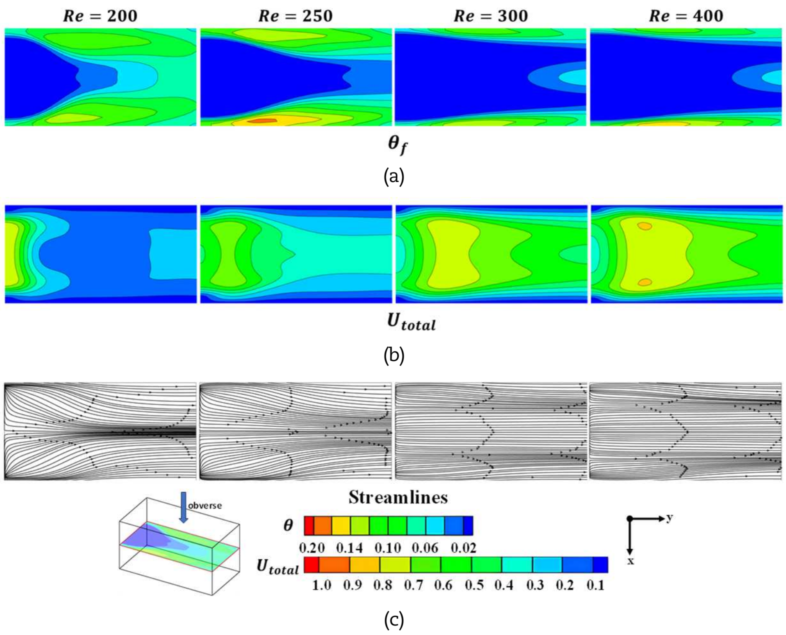

Fig. 10. Effect of Reynolds number on (a) temperature distributions of the fluid, (b) velocity distributions of the fluid and (c) streamlines for ε = 0.4 and h = n/2 at x-y observation section (interface).

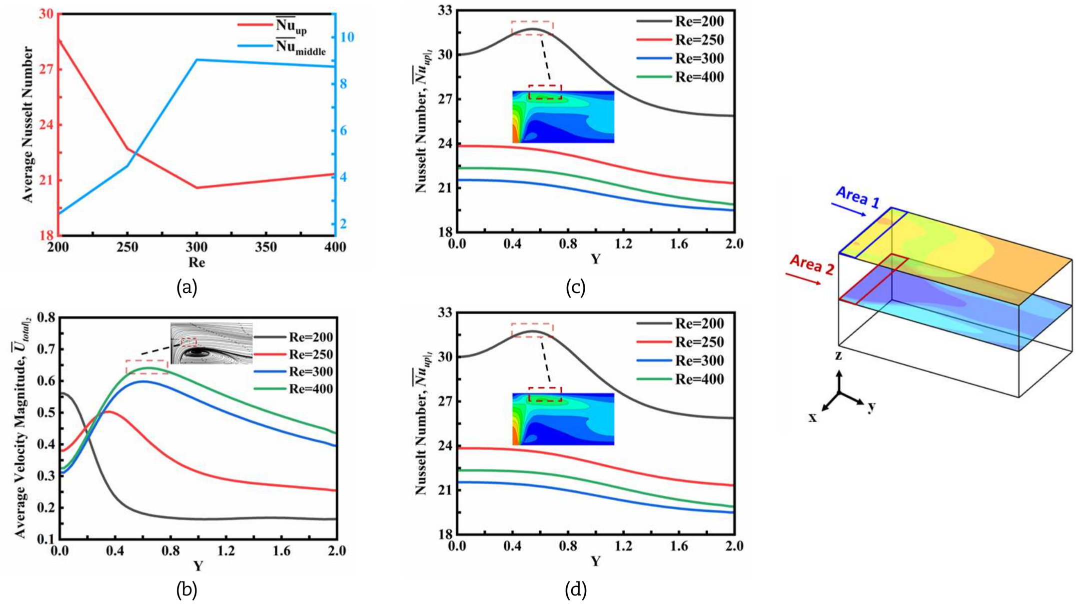

Fig. 11. Effect of Reynolds number on (a) variation in average Nusselt number, (b) variation of velocity magnitude with Y-axis at interface, (c) variation of local Nusselt number with Y-axis at upper surface and (d) variation of local Nusselt number with Y-axis at interface for ε = 0.4 and h = n/2.

To further investigate the flow and heat transfer characteristics at the conjugate heat transfer interface between the porous medium and the free-flow region, Fig. 10 illustrates the temperature and flow fields at the interface. At lower Reynolds numbers (Re = 200), the overall fluid temperature increases along the Y-axis because of the influence of the slot jet and the heat flux density on the upper surface. Meanwhile, at the interface, because of the lower velocity, more cooling medium flows into the porous medium rather than being deflected. Therefore, for lower Reynolds number conditions, vortices are formed in the region of the vertical inlet jet, with faster flow speeds, enhancing convective heat transfer. It presents a low-temperature, high-speed conical region in the temperature and velocity fields. However, for other conditions (Reynolds number: 250-400), as the Reynolds number increases, the fluid impacting on the porous medium is more likely to be deflected, the flow rate in the middle of the interface is faster, so that the formation of the streamlines shifted to both sides. This also leads to more low-temperature areas in the middle of the temperature field, with high-temperature areas being "squeezed" to both sides of the front and rear walls, and the low-temperature and high-speed "conical" areas gradually changing into "rectangular" areas.

Figure 11 contains curve graphs of Nusselt number and velocity magnitude variations at the upper surface and the interfaces of the cavity under different Reynolds numbers. Consistent with the previous section, two typical areas shown in Fig. 11 were selected to study the local Nusselt number and local velocity magnitude. Figure 11(a) reveals a curve graph of the average Nusselt number versus Reynolds number for the upper surface and the interface of the square cavity. In Fig. 11(a), it can be seen that as the Reynolds number is increased from 200 to 400, the average Nusselt number of the upper surface decreases from 28.8 to 21.3, while the average Nusselt number of the interface increases from 2.92 to 8.74, which is the opposite trend. The increase of Reynolds number makes it easier for the fluid to be deflected after impacting the porous medium, which strengthens the convective heat transfer at the interface. However, less fluid enters the top part of the square cavity, the flow rate decreases, and the convective heat transfer at the upper surface is weakened, thus showing a decrease in the average Nusselt number on the upper surface and an increase in the average Nusselt number at the interface. It is noteworthy that when the Reynolds number is increased from 250 to 300, the upper surface average Nusselt number and the interfacial average Nusselt number change most drastically. Observing the flow field in the internal cross section of the square cavity (Fig. 9(c)), the upper surface flow velocity decreases significantly and the interfacial flow velocity increases significantly with the Reynolds number transitions from 250 to 300. This is because at 250 Reynolds number, the fluid deflection tendency is not so obvious, and there is still a lot of fluid entering the upper part of the square cavity for percolation. The variation of the flow field in the square cavity causes the average Nusselt number at the upper surface to increase and the average Nusselt number at the interface to decrease rapidly.

Figure 11(b) demonstrates the variation curve of the interfacial velocity magnitude along the Y-axis for different Reynolds numbers. For Reynolds numbers 250-400, the velocity magnitude at the interface increases to a peak along the Y-axis and then decreases. However, for Reynolds number 200, the velocity magnitude at the interface reaches a peak from the beginning and then decreases all the way. The reason for this trend is that for higher Reynolds number conditions, in the region above inlet, the jet fluid is deflected after contacting the porous medium before vortices generating; and as the vertical distance away from the inlet increases, the vortices are fully developed, and the velocity on interface reaches the peak value. However, for the case of $Re = 200$, in the area perpendicular to the jet inlet, the fluid is hardly deflected, most of the fluid is injected vertically into the porous medium and then percolates. These trends are verified in the streamlines diagram of the z-y observed surfaces. As observed in Fig. 11(c), as mentioned before, the upper surface Nusselt number decreases with the increase of Reynolds number, and for the case of $Re = 200$, the local Nusselt number of the upper surface peaks in the region of Y = 0.6 due to the influence of standing point effect that strengthens the disturbance of the thermal boundary layer. For the other cases, the flow velocity near the upper surface region is low and the velocity magnitude decreases along the direction of the exit, so the local Nusselt number here shows a decreasing trend all the time. Figure 11(d) demonstrates the variation curve of the local Nusselt number with the Y-axis at the interface, in which it can be seen that for all the conditions, the local Nusselt number at the interface shows an overall decreasing trend. Meanwhile, for higher Reynolds number cases, due to the full development of vortices, more intense fluctuation of the local Nusselt number is found. It should be noted that for Reynolds number of 300 and 400, the velocity magnitude at the interface is close to each other, resulting in nearly equal local Nusselt number at the interface.

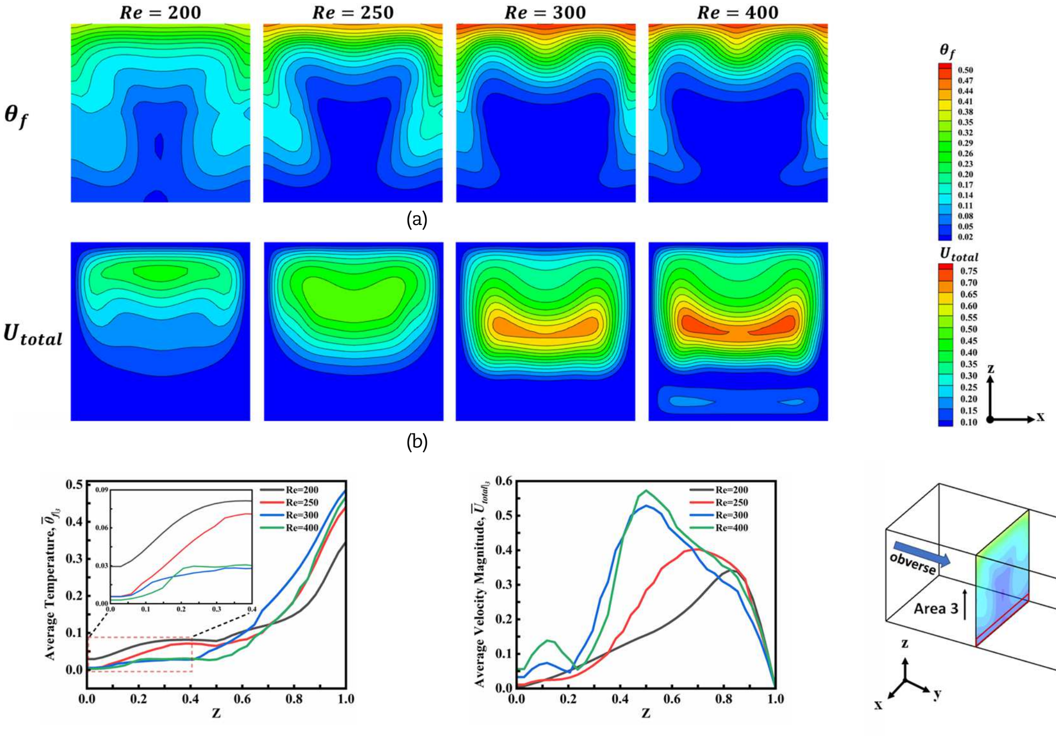

Fig. 12. Effect of Reynolds number on (a) temperature distributions of the fluid, (b) velocity distributions of the fluid, (c) variation of fluid temperature with Z-axis and (d) variation of velocity magnitude with Z-axis for ε = 0.4 and h = n/2 at z-x observation section.

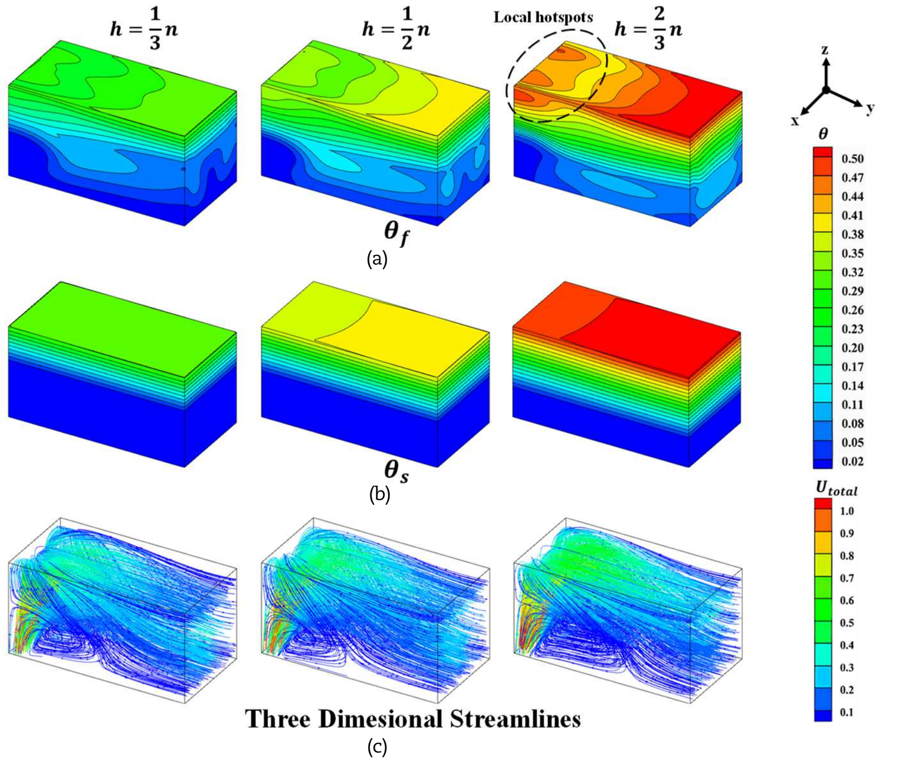

Fig. 13. Effect of porous region thickness on (a) three-dimensional temperature distributions of the fluid, (b) three-dimensional temperature distributions of porous medium and (c) three-dimensional streamlines for ε = 0.4 and Re = 200.

Moreover, the effect of Reynolds number on the flow and heat transfer in the direction perpendicular to the Y-axis is also focused in the study, and z-x observation section inside the square cavity are selected for analysis. Figures 12(a) and 12(b) show the fluid temperature and velocity fields inside the square cavity perpendicular to the Y-axis (Y = 1) observation plane. Figures 12(c) and 12(d) manifest the variation curves of temperature and velocity magnitude of the area 3 shown in schematic diagram of Fig. 12 along the Z-axis. Observation of Fig. 12(a) reveals that as the Reynolds number increases, the higher the temperature at the top of the square cavity, the larger the low temperature channel formed in the middle of the square cavity. It can also be observed in conjunction with Figs. 12(a) and 12(c) that for Reynolds number 300 and 400 conditions, the fluid ejected from the slot has a higher flow rate and tends to be deflected in the middle of the square cavity. This results in a more consistent temperature distribution between the both, with higher temperatures at the top of the square cavity and a large low-temperature region in the middle and lower part of the cavity ($Z < 0.6$). It corresponds to Fig. 11(a) that their upper surface local Nusselt number and interface local Nusselt number values are close to each other. However, comparing the cases of Reynolds number 250 and Reynolds number 300, it can be clearly seen that when the Reynolds number is shifted from 250 to 300, the temperature in the upper part of the square cavity is obviously increased, the temperature gradient becomes larger (the red region increases, and isotherms become denser), and the low-temperature channel in the middle part of the square cavity is obviously widened. This corresponds to the phenomenon of a sudden decrease in the local Nusselt number of the upper surface and a surge of the local Nusselt number of the interface on Fig. 11(a). As seen in the flow field of Fig. 12(b), under the combined action of the jet inlet and porous medium, the Reynolds number increases, causing the region with faster velocity in the square cavity to shift downwards. Figures 12(b) and 12(d) indicate that because of the increase in the jet flow velocity, the cases with Reynolds number 300 and 400 reach the peak velocity in the middle of the square cavity ($Z = 0.5$) and the magnitude of the peak is significantly higher than the other cases. It is worth pointing out that in the curves of Fig. 12(d), these two conditions have small wave peaks with larger velocities in the region of $Z < 0.2$. This is because for the larger Reynolds number case, the fluid deflection is more likely to occur earlier, and the more likely to form a high-speed channel in the middle of the square cavity. At the same time, the formation of the high-speed channel drives the flow velocity of the fluid in the lower part of the square cavity, making the vortex generated in the bottom become flat and long, which is more obvious in the flow field (Fig. 9(c) and Fig. 12(b)) and flow velocity graphs (Fig. 12(d)) for $Re = 400$.

4.3. Effects of porous region thickness

The third section explores the effect of the porous region thickness on the flow and heat transfer inside the square cavity under $\varepsilon = 0.4$ and $Re = 200$ operating conditions. Figure 13 shows the flow and temperature field distributions in three dimensions, and Figures 14 and 15 show the flow and temperature field distributions in two observation sections, respectively.

Figures 13(a) and 13(b) demonstrate the three-dimensional temperature distribution of the fluid and the porous medium, respectively. Comparing Fig. 13(a) and Fig. 13(b), it can be seen that because of the flow characteristics of the fluid, the temperature distribution of the fluid is more uneven. At the same time, due to the influence of the slot jet and the heat flux on the upper surface, the temperature of the fluid gradually increases along the direction of the Y-axis (outlet), whereas the distribution of the temperature field of the porous medium is more homogeneous, and its isotherms are changing in a regular manner. Meanwhile, it can be clearly observed in the temperature distribution contours of the both that the overall temperature of the square cavity increases with the increase of the thickness of the porous layer, and the thermal boundary layer at the top of the square cavity becomes thicker and the temperature gradient becomes larger. This is because the thermal conductivity of foam copper porous media is relatively high, and the thicker the porous layer is, the easier it is to transfer heat to the lower part of the square cavity, thus increasing the overall temperature of the square cavity. It is worth pointing out that in Fig. 13(a), for all the conditions, due to the stagnation point effect inhibiting the development of the thermal boundary layer, the temperature is lower in the region perpendicular to the inlet, and then the temperature of the fluid gradually increases along the outlet direction.

However, for the case of $h = 2n/3$, a local hotspot appeared in the region perpendicular to the jet inlet at the top of the square cavity, which was attributed to the increase of the thickness of the porous layer enhanced the percolation effect of the porous medium, and the stagnation point effect was weakened, so that the heat could not be discharged in time. Additionally, as can be seen from Eq. (22), intermixed percolation of fluids within the porous medium can enhance heat transfer, and this enhancement effect is related to local flow velocity. In the region perpendicular to the jet inlet, where flow velocity is higher, the heat transfer enhancement effect is more pronounced. Meanwhile, combined with the high thermal conductivity of foam copper metal, heat flow of upper surface is more easily transmitted downward. These factors all contribute to the further formation of local hotspots. As shown in the three-dimensional flow diagram of Fig. 13(c), the increase in the thickness of the porous layer makes the streamlines in the upper part of the square cavity denser and in the middle part of the square cavity sparser. This indicates that in the upper part of the square cavity, the flow velocity is faster and the fluid flow is more intense, while in the lower part of the square cavity, the flow velocity is slower and the fluid flow is stable. Especially for the case of $h = n/3$, it can be clearly observed that the streamlines in the middle of the square cavity are the most dense, the flow velocity is faster, and the vortex generated in the front and rear wall is smaller. For other cases, with the increase of the thickness of the porous layer, the influence of the percolation effect of the porous medium is more sufficient and more obvious. This makes the streamlines in the upper part of the square cavity become more denser, and the vortex on the wall surface becomes larger and longer.

In order to further investigate the effect of the change the thickness of the porous region on the flow and heat transfer characteristics inside the square cavity, z-y and x-y observation sections inside the square cavity are selected for the analytical study. Figure 14 shows the temperature field and flow field on the z-y observation section within the square cavity. The same conclusions as in Fig. 13 can be observed in Figs. 14(a) and 14(b): the temperature distribution of the fluid is more dispersed, while the temperature field of the porous medium is more uniformly distributed. In addition, with the increase of the thickness of the porous layer, it is easier for the heat of the porous medium to be transferred to the fluid, and the top thermal boundary layer becomes thicker, with the temperature gradient becoming larger. Differently, comparing Fig. 14(a) and Fig. 13(a), it can be clearly observed that inside the square cavity, the temperature field at the z-y observation section displays more low-temperature regions. Especially for the $h = 2n/3$ case, in the area perpendicular to the jet inlet on its upper surface, local hotspots decrease and the temperature in the lower part of the square cavity decreases. This is because the fluid inside the square cavity is less affected by the front and rear wall surfaces, and the internal vertical jet can enter the square cavity at a faster speed so that more low-temperature fluid can enter the porous media above, enhancing convective heat transfer. Figures 14(c) and 14(d) show the flow field and streamlines of the z-y observation section. Figure 14(c) indicates that as the thickness of the porous layer increases, more fluid can enter the porous medium, the percolation effect of the porous medium is enhanced, and the high-speed region formed in the square cavity is more likely to be deflected to the upper part. The formation of the high-speed region leads to the accumulation of heat and the increase of the fluid temperature. As shown in Fig. 14(d), the change in the thickness of the porous region has a significant effect on the strength of the main vortex, and the increase in the thickness of the porous layer enhances the percolation effect, the vortex is fully developed, and the main vortex becomes larger, which is most obvious when the thickness of the porous layer is in the transition from $n/2$ to $2n/3$. Meanwhile, in the lateral comparison in Fig. 14(d), for the case of $h = n/3$, the effect of percolation is not obvious, the streamlines inside the square cavity shows a clear downward trend. For other cases, the percolation effect is strengthened, and the trend of the streamlines decreases slower, and the streamlines in the upper part of the square cavity becomes denser to form a high-speed region.

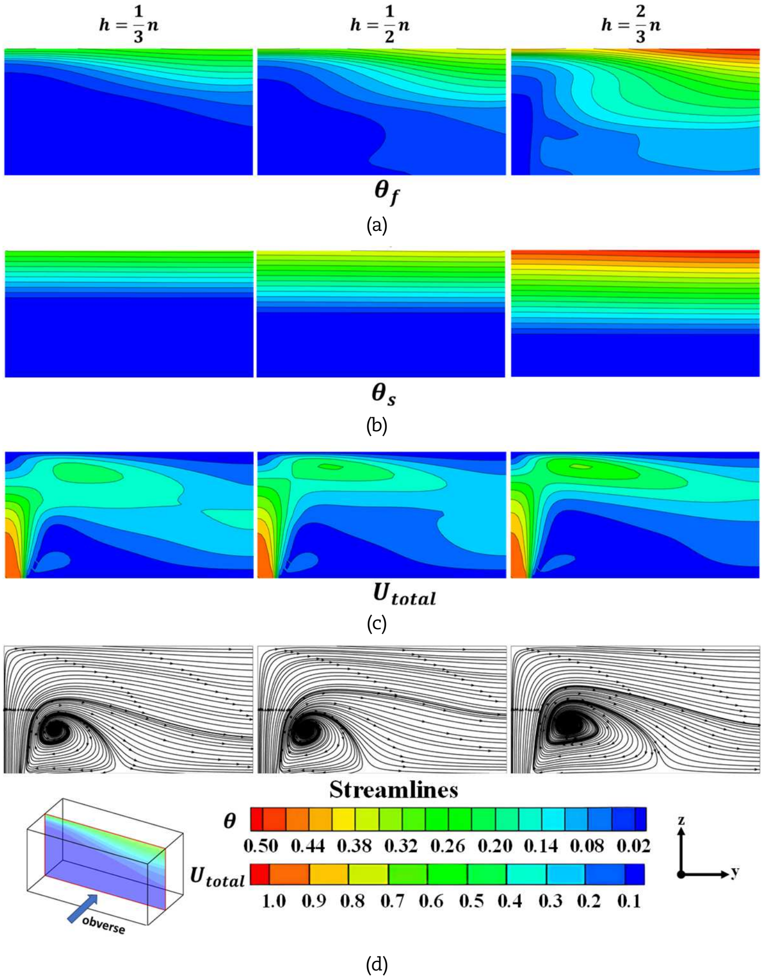

Fig. 14. Effect of porous region thickness on (a) temperature distributions of the fluid, (b) temperature distributions of porous medium, (c) velocity distributions of the fluid and (d) streamlines for ε = 0.4 and Re = 200 at z-y observation section.

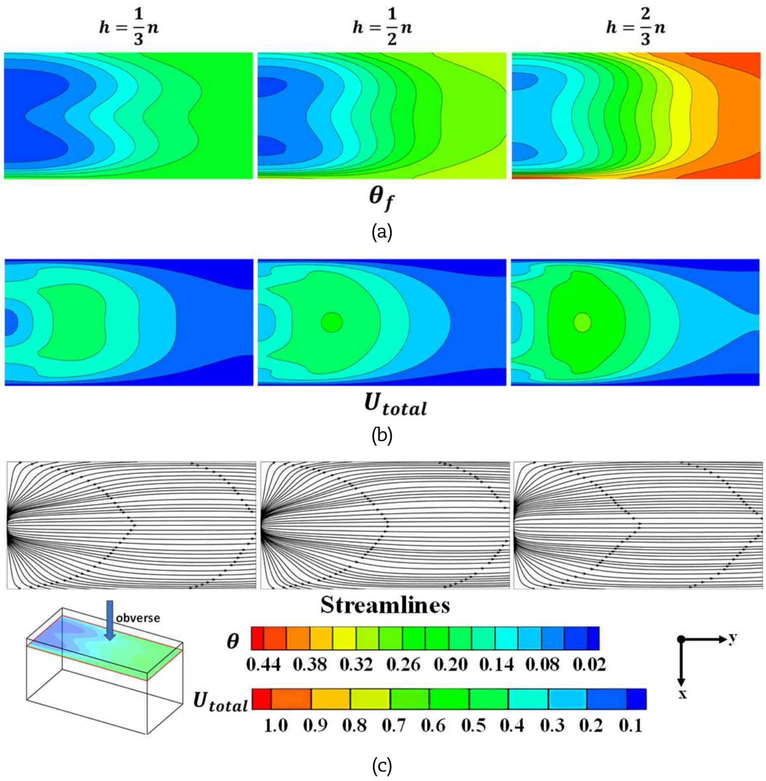

Fig. 15. Effect of porous region thickness on (a) temperature distributions of the fluid, (b) velocity distributions of the fluid and (c) streamlines for ε = 0.4 and Re = 200 at x-y observation section (h = n/6).

Based on the flow characteristics inside the square cavity, the x-y observation section near the upper surface ($h = n/6$) is selected to study the effect of thickness of the porous region on the flow and temperature fields inside the square cavity. In Fig. 15(a), it can be seen that under the influence of the slot jet and the continuous heat flow on the upper surface, the fluid temperature increases along the Y-axis as a whole. In addition, because heat transfer dominates at the top of the square cavity, with the thickness of the porous layer increases, the easier it is to transfer heat from the upper surface along the copper foam to the lower part of the square cavity. At the same time, the thicker the porous layer, the faster the flow rate in the upper part of the square cavity, the convective heat transfer is enhanced, and the upper fluid receives more heat. This resulted in an increase of the fluid temperature in the region near the upper surface of the square cavity. It is worth pointing out that in the simulation, the front and rear wall surfaces (X direction) of the square cavity are set as adiabatic and stationary wall surfaces, which makes the low-temperature fluid entering from the jet inlet stagnate and accumulate heat after contacting the wall surfaces, forming a low-temperature and high-speed region in the middle of the square cavity. This results in the phenomenon of low temperature in the middle and high temperature at the front and rear wall surfaces. Figure 15(b) shows the velocity field of the fluid at the $h = n/6$ x-y observation section, as shown, the flow velocity in the upper part of the square cavity increases with the increasing thickness of the porous layer, and the velocity field of the fluid exhibits more regions of high velocity (green part). It should be noted that comparing the velocity field at the interface (Figs. 5(b) and 10(b)), there is a region of lower flow velocity on the left side of the flow field in Fig. 15(b) (blue semi-circular region). This is because the fluid near the upper surface region of the square cavity is exposed to more porous media compared to the interfacial region perpendicular to the jet inlet. Meanwhile, the fluid is more likely to flow into the porous media, the seepage effect is more pronounced, resulting localised flow velocity reduction on the left side, which are verified in the streamlines in Fig. 15(c). As shown in Fig. 15(c), as the thickness of the porous layer increases, there are more straight streamlines in the middle of the square cavity, and more fluid can flow at a faster rate to the outlet, thus the velocity field exhibits more high-speed regions.

Figure 16 contains curve graphs of Nusselt number and velocity magnitude variations for the upper surface of the cavity and the $h = n/6$ surface under different porous layer thickness. Consistent with the previous text, two typical areas shown in Fig. 16 were selected to study the local Nusselt number and local velocity magnitude. Figure 16(a) provides a combined analysis of the average Nusselt number for the upper surface and the $h = n/6$ surface. When the thickness of the porous region is increased from $n/3$ to $2n/3$, the average Nusselt number on the upper surface decreases from 36.2 to 22.5, and the average Nusselt number on the $h = n/6$ surface decreases from 2.26 to 1.43, which show the same trend of change, and the curves of the variation of Nusselt number are more similar. This indicates that the heat conduction of the porous medium dominates at the upper surface of the square cavity and its surrounding region, and with the increase of the thickness of the porous layer, the heat flow from the upper surface is more likely to be transferred downwards along the copper foam, resulting in an increase in the temperature of the upper part of the square cavity and a larger temperature gradient.

Figure 16(b) demonstrates the variation trend of $h = n/6$ surface velocity magnitude along the Y-axis for different porous region thicknesses. For all cases, the flow velocities show a tendency to increase to a peak and then decrease. It is worth noting that at the $h = n/6$ surface, the fluid flow velocity peaks in the region near the vertical jet inlet (Y = 0.55 region) due to the combined effect of the jet inlet and the porous media seepage. This tendency corresponds to the cloud diagram of the velocity field. As shown in Fig. 16(c), as analysed previously, the upper surface Nusselt number decreases with the increase of the porous layer thickness. However, due to the stagnation point effect, the vertically injected fluid gradually decelerates after contacting the porous medium and finally comes to rest at the upper wall surface, which strengthens the destruction of the thermal boundary layer. Thus, the local Nusselt number of the upper surface peaks at the Y = 0.55 region, and the fluid flow rate is also faster near this region, enhancing the convective heat transfer. Figure 16(d) shows the variation curve of $h = n/6$ surface local Nusselt number with Y-axis, in which it can be seen that, for all the working conditions, the $h = n/6$ surface local Nusselt number have reached the peak at Y = 0 and then show the overall decreasing trend. It should be pointed out that, unlike the fluctuation of the local Nusselt number on the upper surface due to the stagnation point effect, the fluctuation on the $h = n/6$ surface is due to heat accumulation. The thicker the thickness of the porous layer, the easier it is to form a high-speed channel in the upper part of the square cavity, the generation of the streamlines more straight. At the same time, under the influence of heat exchange between the porous medium and the fluid, the fluid generates heat accumulation, and the fluctuation of the local Nusselt number occurs.

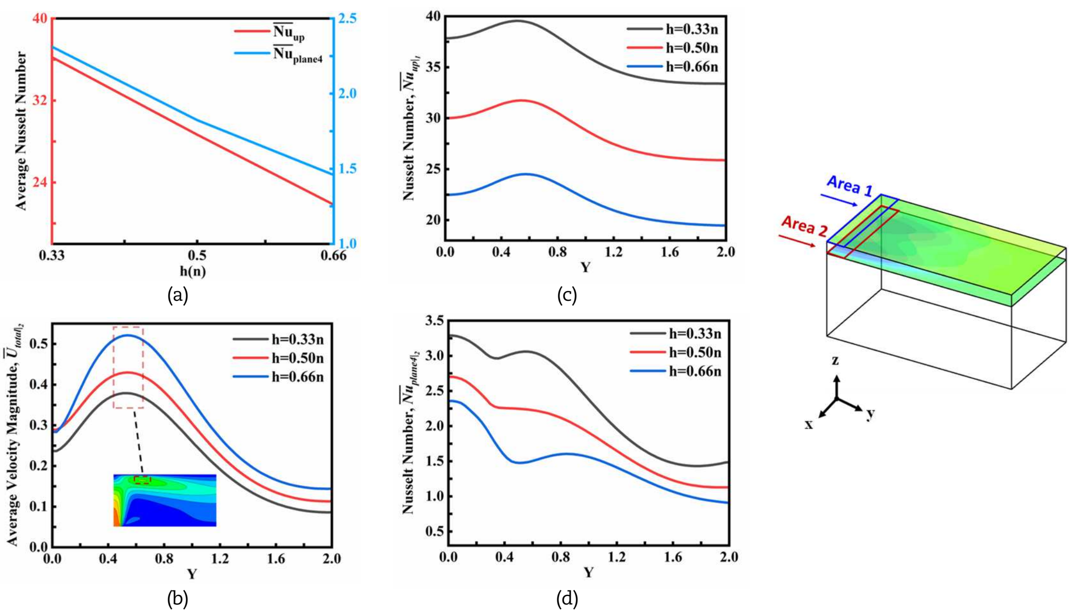

Fig. 16. Effect of porous region thickness (a) variation in average Nusselt number, (b) variation of velocity magnitude with Y-axis at h = n/6 surface, (c) variation of local Nusselt number with Y-axis at upper surface and (d) variation of local Nusselt number with Y-axis at h = n/6 surface for ε = 0.4 and Re = 200.

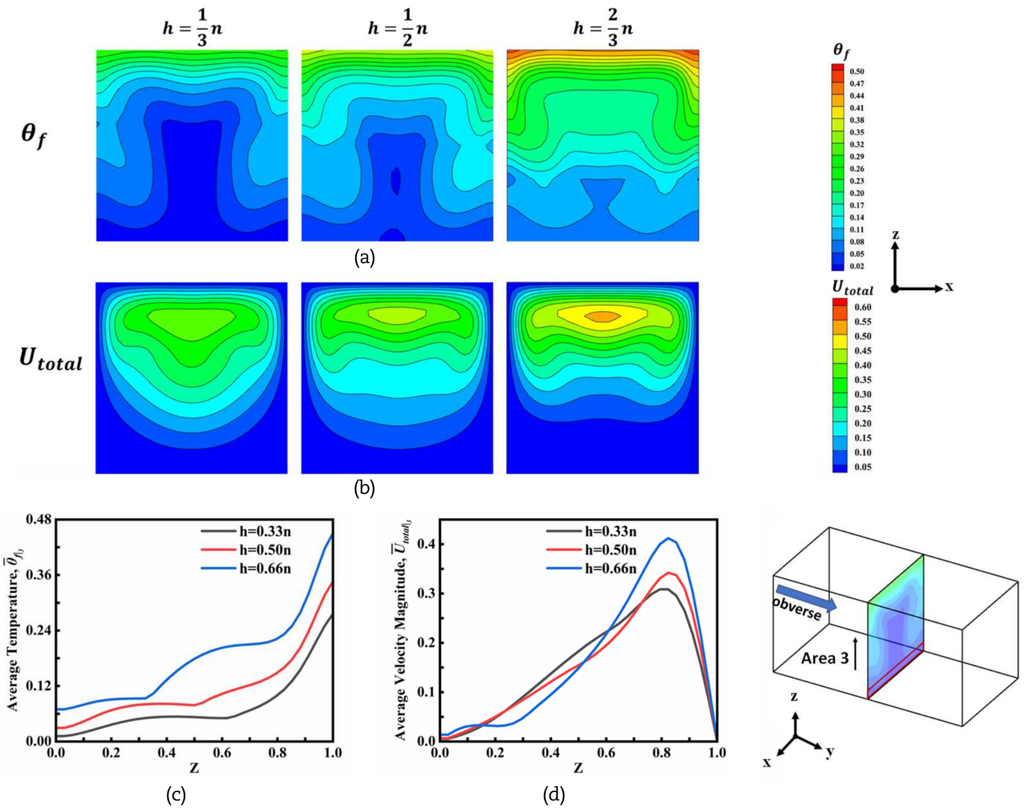

Fig. 17. Effect of porous region thickness on (a) temperature distributions of the fluid, (b) velocity distributions of the fluid, (c) variation of fluid temperature with Z-axis and (d) variation of velocity magnitude with Z-axis for ε = 0.4 and Re = 200 at z-x observation section.

In addition, in order to analyze the flow and heat transfer characteristics inside the square cavity perpendicular to the Y-axis, z-x observation sections inside the square cavity are selected for analytical study. Figures 17(a) and 17(b) manifest the fluid temperature field and velocity field inside the square cavity perpendicular to the Y-axis (Y = 1) observation plane. Figures 17(c) and 17(d) show the variation curves along the Z-axis of the temperature and velocity magnitude of the area 3 shown in schematic diagram of Fig. 17. Combining Fig. 17(a) with 17(c), it can be concluded in agreement with the previous analysis that the fluid temperature and temperature gradient in the upper part of the square cavity increase with the increase of the porous layer, and the closer to the upper surface, the higher the fluid temperature is. Differently, Fig. 17(a) clearly demonstrates the existence of low-temperature channels in the lower part of the square cavity, and the size of the low-temperature channels decreases with the increase of the thickness of the porous layer. It should be noted that above the low-temperature channel, the fluid temperature increases significantly, the isotherm becomes denser, and the temperature gradient becomes larger, and this phenomenon is more and more obvious at the working condition of $h = 2n/3$. As shown in Fig. 17(b) and Fig. 17(d), for all the working conditions, the jet fluid is deflected by the combined action of the porous medium and the upper wall surface, and the velocity peaks in the upper part of the square cavity (Z = 0.8). The difference is that, because of the percolation effect of the porous medium, for conditions with thicker porous layers, the fluid is more likely to flow upward after entering the porous medium from the free flow area. The high-speed channel formed in the upper part of the square cavity has a faster flow velocity, and the fluid heat is easily accumulated, resulting in an increase in temperature. However, for working conditions where the thickness of the porous layer is thin, the high-speed channel formed by the fluid is shifted downwards. The flow velocity in the lower part of the square cavity becomes faster, the vortex formed is smaller, and the easier it is to form a low-temperature channel.

5. Conclusion

In this paper, a three-dimensional mathematical model of microchannel heat sink slot jet partially filled with porous media coupled heat transfer was constructed with the local thermal non-equilibrium (LTNE) model and the Darcy-Forchheimer model, taking into account the buoyancy effect and the conjugate heat transfer boundary conditions. The effects of porosity, Reynolds number and thickness of the porous region on the flow and temperature fields were comprehensively evaluated by numerical simulations. The main conclusions are as follows:

- For the square cavity partially filled with porous media slot jet, the fluid temperature distribution is more dispersed, while the temperature field of the porous medium is more uniformly distributed, and its isotherms are regularly varying. The temperature is lower in the region perpendicular to the jet inlet and gradually increases along the outlet direction (Y-axis) because of the stagnation point effect of the jet impact, which disturbs the thermal boundary layer in the upper part of the square cavity. The change in porosity does not strongly affect the flow behaviour of the fluid and the main vortex intensity increases slightly with increasing porosity. However, the greater the porosity, the less foam copper, which increases the heat flow directly acting on the fluid on the upper surface of the square cavity, and the overall temperature of the square cavity increases. Meanwhile, the average Nusselt number on the upper surface and interface shows an opposite trend.
- The change of Reynolds number strongly affects the flow behaviour of the fluid, as the Reynolds number increases, the high-speed fluid impacting the porous medium is more likely to produce deflection, the flatter and longer the vortex formed. For Reynolds numbers of 300 and 400, the strong deflection tendency of the fluid causes a large area of high-speed cryogenic channels to form in the center of the square cavity. These phenomena result in an opposite trend of decreasing the average Nusselt number at the upper surface from 28.8 to 21.3 as the Reynolds number was increased from 200 to 400, while the

average Nusselt number at the interface increases from 2.92 to 8.74. Meanwhile, when the Reynolds number is increased from 250 to 300, the both change most drastically.

- As the thickness of the porous layer increases, making the streamlines in the upper part of the square cavity become dense, and the streamlines in the middle part of the square cavity become sparse, and the vortex generated becomes larger and longer. Meanwhile, because of the high thermal conductivity of copper foam, with the increase of the thickness of the porous layer, the heat of the porous medium can be easily transferred to the fluid, leads to an increase in the overall temperature of the square cavity. These phenomena result in an opposite trend of decreasing the average Nusselt number on the upper surface from 36.2 to 22.5 as the thickness of the porous region is increased from n/3 to 2n/3, while the average Nusselt number on the surface with h = n/6 increases from 2.92 to 8.74.

Author Contributions

H. Pan developed the mathematical modeling, conducted the theoretical validation, and analyzed the empirical results; Y. Zhuang undertook writing, review, editing, and supervision; designed the methodology; W. Fan performed the conceptualization, review and supervision; F. Zhong performed the conceptualization, review and supervision. All authors discussed the results, reviewed the manuscript, and approved the final version.

Acknowledgments

The authors are very grateful for the reviewers' comments, and editors' recommendations through which the revision of the work has been improved with effective presentation of the research paper.

Conflict of Interest

We declare that we have no conflict of interest.

Funding

We would like to acknowledge the Grant support from the Opening Project (2023KF12) of the State Key Laboratory of High Temperature Gas Dynamics, National Natural Science Foundation of China (52476063 and 52006039), and Natural Science Foundation of Guangdong Province (2023A1515012937).

Data Availability Statements

The datasets generated and/or analyzed during the current study are available from the corresponding author on reasonable request.

Nomenclature

a_{sf}	Interfacial surface area	c	Specific heat capacity
C	Inertial coefficient	d_f	Fiber diameter
d_p	Pore size	d_k	Characteristic length
Da	Darcy number	g	gravitational acceleration
Gr	Grashof number	h	Thickness of porous layer
h_{sf}	Interfacial heat transfer coefficient	H	Dimensionless interphase heat transfer coefficient
k	thermal conductivity	k_{td}	Thermal dispersion conductivity
K	Permeability	n	Square cavity size
m	Current iteration step	Nu	Nusselt number
p	Pressure	P	Non-dimensional pressure
Pr	Prandtl number	q_w	Upper surface heat flow
Re	Reynolds number	T	Temperature
t	Time	u	X-velocity component
U	Non-dimensional X-velocity component	v	V-velocity component
V	Non-dimensional V-velocity component	w	W-velocity component
W	Non-dimensional Z-velocity component	x	X-coordinate
X	Non-dimensional X-direction	y	Y-coordinate
Y	Non-dimensional Y-direction	z	Z-coordinate
Z	Non-dimensional Z-direction		

Greek symbols

α	Eff. thermal diffusivity of porous medium & fluid	β	Thermal expansion coefficient
γ	Ratio of thermal conductivity for fluid & copper foam	ε	Porosity of copper foam
θ	Non-dimensional temperature	λ	Porous medium regional control coefficient

μ'	Dynamic viscosity coefficient	ξ	Effective thermal diffusivity ratio for liquid & copper foam
Φ	Dependent variable	ρ	Density
τ	Non-dimensional time	υ	Kinematic viscosity coefficient
χ	Tortuosity coefficient	ω	Pore density of copper foam
Subscripts			
eff	Effectiveness	*f*	Liquid
fe	Effectiveness of liquid	*in*	Inlet
s	Porous media (copper foam)	*se*	Effectiveness of porous media
∞	External environment	$+$	Relevant parameters of the fluid
$-$	Relevant parameters of the porous		

References

[1] Hamidnia, M., Luo, Y., Wang, X.D., Application of micro/nano technology for thermal management of high power LED packaging - A review, *Applied Thermal Engineering*, 145, 2018, 637-651.
[2] Singh, A.K., Dey, S., McDonald-Maier, K., Basireddy, K.R., Merrett, G.V., Al-Hashimi, B.M., Dynamic Energy and Thermal Management of Multi-core Mobile Platforms: A Survey, *IEEE Design & Test*, 37(5), 2020, 25-33.
[3] Chen, H., Abidi, A., Hussein, A.K., Younis, O., Degani, M., Heidarshenas, B., Investigation of the use of extended surfaces in paraffin wax phase change material in thermal management of a cylindrical lithium-ion battery: Applicable in the aerospace industry, *Journal of Energy Storage*, 45, 2022, 103685.
[4] Zhong, N., Chen, M., Luo, Y., Wang, Z., Xin, X., Rittmann, B.E., A novel photocatalytic optical hollow-fiber with high photocatalytic activity for enhancement of 4-chlorophenol degradation, *Chemical Engineering Journal*, 355, 2019, 731-739.
[5] Electronics Manufacturing Initiative Technology Roadmap, iNEMI, 2004.
[6] Gong, L., Xu, Y.P., Ding, B., Zhang, Z.H., Huang, Z.Q., Thermal management and structural parameters optimization of MCM-BGA 3D package model, *International Journal of Thermal Sciences*, 147, 2020, 106120.
[7] He, Z., Yan, Y., Zhang, Z., Thermal management and temperature uniformity enhancement of electronic devices by micro heat sinks: A review, *Energy*, 216, 2021, 119223.
[8] Zhang, J., Wu, X., Zhou, D., Li, Q.-Y., Li, X., Chen, K., Experimental and numerical investigation on efficient optimization of battery thermal management systems, *Applied Thermal Engineering*, 221, 2023, 119821.
[9] Tuckerman, D.B., Pease, R.F.W., High-performance heat sinking for VLSI, *IEEE Electron Device Letters*, 2(5), 1981, 126-9.
[10] Li, Y.T., Gong, L., Xu, M.H., Joshi, Y., Hydraulic and thermal performances of metal foam and pin fin hybrid heat sink, *Applied Thermal Engineering*, 166, 2020, 114665.
[11] Huang, C.-H., Tung, P.-W., Numerical and experimental studies on an optimum Fin design problem to determine the deformed wavy-shaped heat sinks, *International Journal of Thermal Sciences*, 151, 2020, 106282.
[12] Moradikazerouni, A., Heat transfer characteristics of thermal energy storage system using single and multi-phase cooled heat sinks: A review, *Journal of Energy Storage*, 49, 2022, 104097.
[13] Xie, H., Wang, T., ELSihy, E.S., Lin, H., Wang, Z., Investigation on the thermal and hydrodynamic performance of a microchannel heat sink partially filled with porous medium, *International Journal of Heat and Mass Transfer*, 228, 2024, 125627.
[14] Sidik, N.A.C., Muhamad, M.N.A.W., Japar, W.M.A.A., Rasid, Z.A., An overview of passive techniques for heat transfer augmentation in microchannel heat sink, *International Communications in Heat and Mass Transfer*, 88, 2017, 74-83.
[15] Dixit, T., Ghosh, I., Review of micro- and mini-channel heat sinks and heat exchangers for single phase fluids, *Renewable & Sustainable Energy Reviews*, 41, 2015, 1298-1311.
[16] Mudhafar, M.A.H., Xu, Y.-F., Fluid flow and heat transfer characteristics on uncoated and micro porous straight and divergent heat exchangers for high-powered electronic devices, *Heat and Mass Transfer*, 59(4), 2023, 599-619.
[17] Naphon, P., Khonseur, O., Study on the convective heat transfer and pressure drop in the micro-channel heat sink, *International Communications in Heat and Mass Transfer*, 36(1), 2009, 39-44.
[18] van Erp, R., Soleimanzadeh, R., Nela, L., Kampitsis, G., Matioli, E., Co-designing electronics with microfluidics for more sustainable cooling, *Nature*, 585(7824), 2020, 211-+.
[19] Pan, Y.H., Zhao, R., Fan, X.H., Nian, Y.L., Cheng, W.L., Study on the effect of varying channel aspect ratio on heat transfer performance of manifold microchannel heat sink, *International Journal of Heat and Mass Transfer*, 163, 2020, 120461.
[20] Naqiuddin, N.H., Saw, L.H., Yew, M.C., Yusof, F., Ng, T.C., Yew, M.K., Overview of micro-channel design for high heat flux application, *Renewable & Sustainable Energy Reviews*, 82, 2018, 901-914.
[21] Chai, L., Xia, G.D., Wang, H.S., Laminar flow and heat transfer characteristics of interrupted microchannel heat sink with ribs in the transverse microchambers, *International Journal of Thermal Sciences*, 110, 2016, 1-11.
[22] Chai, L., Xia, G.D., Wang, H.S., Numerical study of laminar flow and heat transfer in microchannel heat sink with offset ribs on sidewalls, *Applied Thermal Engineering*, 92, 2016, 32-41.
[23] Chai, L., Xia, G.D., Wang, H.S., Parametric study on thermal and hydraulic characteristics of laminar flow in microchannel heat sink with fan-shaped ribs on sidewalls - Part 3: Performance evaluation, *International Journal of Heat and Mass Transfer*, 97, 2016, 1091-1101.
[24] Chen, Y., Zhuang, Y., Feng, J.-C., Huang, S.-M., Numerical investigation on flow and heat transfer characteristics in honeycomb-like microchannel heat sink encapsulated with phase change material, *Applied Thermal Engineering*, 232, 2023, 121060.
[25] Sempertegui-Tapia, D.F., Ribatski, G., The effect of the cross-sectional geometry on saturated flow boiling heat transfer in horizontal micro-scale channels, *Experimental Thermal and Fluid Science*, 89, 2017, 98-109.
[26] Zheng, L., Zhang, D., Xie, Y., Xie, G., Thermal performance of dimpled/protruded circular and annular microchannel tube heat sink, *Journal of the Taiwan Institute of Chemical Engineers*, 60, 2016, 342-351.
[27] Muszynski, T., Andrzejczyk, R., Heat transfer characteristics of hybrid microjet - Microchannel cooling module, *Applied Thermal Engineering*, 93, 2016, 1360-1366.
[28] Peng, M., Chen, L., Ji, W., Tao, W., Numerical study on flow and heat transfer in a multi-jet microchannel heat sink, *International Journal of Heat and Mass Transfer*, 157, 2020, 119982.
[29] Shen, H., Gao, S.Y., Lan, X.Y., Liu, H.L., Xie, G.N., Wang, C.C., Performance of impingement-jet double-layer nested microchannel heat sinks with vertical central bifurcation-A numerical approach and experimental verification, *International Journal of Heat and Mass Transfer*, 222, 2024, 125203.
[30] Shen, H., Lan, X.Y., Xie, G.N., Wang, C.C., Parametric study for thermal uniformity analysis on vertical fin located in novel designed impacting-jet double-layer nested microchannel heat sinks verified by SLM 3D printing method, *International Communications in Heat and Mass Transfer*, 159, 2024, 108321.
[31] Gao, W., Zhang, J.F., Qu, Z.G., Tao, W.Q., Numerical investigations of heat transfer in hybrid microchannel heat sink with multi-jet impinging and trapezoidal fins, *International Journal of Thermal Sciences*, 164, 2021, 106902.
[32] Zhang, Y., Wang, S., Ding, P., Effects of channel shape on the cooling performance of hybrid micro-channel and slot-jet module, *International Journal of Heat and Mass Transfer*, 113, 2017, 295-309.
[33] Sun, W., Li, P., Zhou, T., Li, Y.T., Li, C.C., Shao, X.D., Shen, H., Thermo-fluids performance analysis and experimental verification of topologically

optimized mini-channel heat sinks integrated with impact jet, *International Journal of Thermal Sciences*, 211, 2025, 109705.
[34] Buonomo, B., Manca, O., Lauriat, G., Forced convection in micro-channels filled with porous media in local thermal non-equilibrium conditions, *International Journal of Thermal Sciences*, 77, 2014, 206-222.
[35] Jeng, T.-M., Tzeng, S.-C., Height effect on heat transfer characteristics of sintered porous blocks with a confined slot jet, *International Communications in Heat and Mass Transfer*, 35(1), 2008, 30-38.
[36] Xu, W., Huang, T., Huang, S.-M., Zhuang, Y., Regulation mechanism of magnetic field on non-Newtonian melting and energy storage performance of metal foam composite nano-enhanced phase change materials, *International Journal of Heat and Mass Transfer*, 200, 2023, 123501.
[37] Xu, W., Huang, Z., Zhuang, Y., Feng, J.-C., Thermocapillary convection modes and phase change heat transfer characteristics of three-dimensional metal foam composited phase change materials with different aspect ratios under microgravity, *International Journal of Heat and Mass Transfer*, 222, 2024, 125155.
[38] Zhuang, Y., Huang, T., Feng, J.-C., Oscillatory instability of magneto-convection during the melting of non-Newtonian ferromagnetic nano-enhanced phase change materials at low Rayleigh number, *Applied Thermal Engineering*, 248, 2024, 123306.
[39] Buonomo, B., Lauriat, G., Manca, O., Nardini, S., Numerical investigation on laminar slot-jet impinging in a confined porous medium in local thermal non-equilibrium, *International Journal of Heat and Mass Transfer*, 98, 2016, 484-492.
[40] Hwang, M.-L., Yang, Y.-T., Numerical simulation of turbulent fluid flow and heat transfer characteristics in metallic porous block subjected to a confined slot jet, *International Journal of Thermal Sciences*, 55, 2012, 31-39.
[41] Dorea, F.T., de Lemos, M.J.S., Simulation of laminar impinging jet on a porous medium with a thermal non-equilibrium model, *International Journal of Heat and Mass Transfer*, 53(23-24), 2010, 5089-5101.
[42] Cicek, O., Baytas, A.C., Nanofluid jet impingement heating of a cooled surface with a constant heat flux in the presence of porous layer, *International Journal of Numerical Methods for Heat & Fluid Flow*, 32(2), 2022, 825-849.
[43] Kashkuli, S., Mahjoob, S., Vafai, K., Numerical Analysis of Liquid Jet Impingement through Confined Uniform Cooling Channels Employing Porous Metal Foams, *Transport in Porous Media*, 152(2), 2025, 13.
[44] Hunt, M.L., Tien, C.L., Effects of thermal dispersion on forced convection in fibrous media, *International Journal of Heat and Mass Transfer*, 31(2), 1988, 301-9.
[45] Zhang, X., Su, G., Lin, J., Liu, A., Wang, C., Zhuang, Y., Three-dimensional numerical investigation on melting performance of phase change material composited with copper foam in local thermal non-equilibrium containing an internal heater, *International Journal of Heat and Mass Transfer*, 170, 2021, 121021.
[46] Zhuang, Y., Liu, Z., Xu, W., Effects of gradient porous metal foam on the melting performance and energy storage of composite phase change materials subjected to an internal heater: A numerical study and PIV experimental validation, *International Journal of Heat and Mass Transfer*, 183, 2022, 122081.
[47] Nield A.B., *Convection in Porous Media*, Springer, New York, 2006.
[48] Fourie, J.G., Du Plessis, J.P., Pressure drop modelling in cellular metallic foams, *Chemical Engineering Science*, 57(14), 2002, 2781-2789.
[49] Boomsma, K., Poulikakos, D., On the effective thermal conductivity of a three-dimensionally structured fluid-saturated metal foam, *International Journal of Heat and Mass Transfer*, 44(4), 2001, 827-836.
[50] Georgiadis, J.G., Catton, I., Dispersion in cellular thermal convection in porous layers, *International Journal of Heat and Mass Transfer*, 31(5), 1988, 1081-91.
[51] Zhang, P., Meng, Z.N., Zhu, H., Wang, Y.L., Peng, S.P., Melting heat transfer characteristics of a composite phase change material fabricated by paraffin and metal foam, *Applied Energy*, 185, 2017, 1971-1983.
[52] Žukauskas, A., Heat transfer from tubes in crossflow, *Advances in Heat Transfer*, 8, 1972, 93-160.
[53] Alazmi, B., Vafai, K., Constant wall heat flux boundary conditions in porous media under local thermal non-equilibrium conditions, *International Journal of Heat and Mass Transfer*, 45(15), 2002, 3071-3087.
[54] Costa, M.L., Sampaio, R., da Gama, R.M., Modelling and simulation of energy transfer in a saturated flow through a porous medium, *Applied Mathematical Modelling*, 16, 1992, 589-597.
[55] Mattos, H.C., Costa, M.M., Sampaio, R., da Gama, R.S., A thermodynamically consistent constitutive theory for a rigid solid-stokesian fluid mixture, *Mechanics Research Communications*, 20, 1993, 243-249.
[56] Vafai, K., Thiyagaraja, R., Analysis of flow and heat transfer at the interface region of a porous medium, *International Journal of Heat and Mass Transfer*, 30(7), 1987, 1391-1405.
[57] Martins-Costa, M.L., Saldanha de Gama, R.M., A local model for the heat transfer process in two distinct flow regions, *International Journal of Heat and Fluid Flow*, 15(6), 1994, 477-85.
[58] Xu, W., Liu, Z., Huang, S.M., Zhuang, Y., Evaluation and development of a predictive model for conjugate phase change heat transfer of energy storage system partially filled with porous media, *Energy Storage and Saving*, 1, 2022, 293-308.
[59] Zhuang, Y.J., Zhu, Q.Y., Numerical study on combined buoyancy-Marangoni convection heat and mass transfer of power-law nanofluids in a cubic cavity filled with a heterogeneous porous medium, *International Journal of Heat and Fluid Flow*, 71, 2018, 39-54.
[60] Graminho, D.R., de Lemos, M.J.S., Laminar confined impinging jet into a porous layer, *Numerical Heat Transfer Part A-Applications*, 54(2), 2008, 151-177.

ORCID iD

Hongyu Pan https://orcid.org/0009-0008-7209-1788
Yijie Zhuang https://orcid.org/0000-0002-4318-4220
Wenhui Fan https://orcid.org/0000-0002-1018-0258
Fengquan Zhong https://orcid.org/0000-0001-7248-3628

How to cite this article: Pan H., Zhuang Y., Fan W., Zhong F. Effect of Slot Jet on Heat Transfer and Flow Characteristics of Microchannel Heat Sink Partially Filled with Porous Media at High Heat Flow Density and Conjugate Heat Transfer Boundary Conditions, *J. Appl. Comput. Mech.*, 12(1), 2026, 309-330. https://doi.org/10.22055/jacm.2025.48415.5217